RESEARCH ARTICLE

Key Points:
- Log-scaled remanence maps improve resolution of weak-field processes and high-coercivity remanence
- Mineral microstructures and their contribution to IRM can be identified from remanence maps
- Hematite has characteristic signature in log remanence maps resulting from embedded hard moments

Correspondence to:
N. S. Church,
nathan.church@ntnu.no

Nonlinear Preisach maps: Detecting and characterizing separate remanent magnetic fractions in complex natural samples

Nathan S. Church[1], Karl Fabian[2,3], and Suzanne A. McEnroe[1]

[1]Department of Geology and Mineral Resources Engineering, Sem Sælands vei 1, NTNU, Trondheim, Norway, [2]Geological Survey of Norway, Trondheim, Norway, [3]CAGE—Centre for Arctic Gas Hydrate, Environment and Climate, Department of Geology, University of Tromsø, Tromsø, Norway

Abstract Natural remanent magnetization carriers in rocks can contain mixtures of magnetic minerals that interact in complex ways and are challenging to characterize by current measurement techniques. Here a nonlinear mapping scheme is described that efficiently enhances sensitivity and the resolution power of remanent Preisach maps. Using this scheme a large dynamic range of magnetic moments and coercivities can be reliably resolved. The method is applied to synthetic and natural standard samples containing magnetite and hematite, as well as to natural samples from remanent magnetic anomalies where complex microstructures are observed. It is shown that certain offset high-coercivity patterns in remanent Preisach maps may serve as fingerprints for exsolution structures of ilmenite in hematite or hematite in ilmenite and that in some magnetite-bearing remanent anomalies the magnetite coercivity is increased beyond its intrinsic coercivity range. Experimental results and theoretical considerations indicate a minimal coercivity of about 10 mT for single-domain (SD) magnetite, such that observation of lower coercivities implies pseudo-SD (PSD) or multidomain grain sizes. A diagnostic hematite pattern with a peak downward offset of $17 \pm 2\%$ of the intrinsic coercivity is found that is stable over a large range of intrinsic coercivities and may be related to shielding of internal defect or lamellar moments by a spin canting response to the internal field.

1. Introduction

The accurate description of magnetic carriers in rock samples underlies the interpretations in any paleo-magnetism, rock magnetism, or environmental magnetism study. A wide variety of techniques have been developed to measure intrinsic magnetic properties and to infer particle domain state, interactions, and other parameters of complex magnetic systems. Measurements of coercivity are a useful classical tool to characterize properties of distributions of magnetic carriers, which aid interpretation of their origin in rock and environmental magnetic studies and of their stability essential for assessing the validity of paleomagnetic data [*Stacey and Banerjee*, 1974; *Dunlop and Özdemir*, 1997]. For speed of measurement and because it is a more fundamental physical property, these coercivity measurements are usually based on H_c rather than H_{cr} (coercivity of remanence). However, the bulk coercivity of a complex magnetic system is a nonlinear function of both the intrinsic coercivity of the carriers and the total magnetization of each phase or each distribution with a given coercivity profile. Therefore, a strong induced signal will dominate high-field behavior, leaving the remanence signal poorly resolved.

A variety of sophisticated techniques have been adopted in recent years to examine multiphase samples, to characterize the constituent phases, and to infer how the interplay of signals creates bulk behavior. One powerful isothermal technique is the analysis of first-order reversal curve (FORC) diagrams [*Pike et al.*, 1999; *Roberts et al.*, 2000], which can discriminate between magnetic domain states as well as observe magne-tostatic or exchange interactions and identify different magnetic mineralogies [*Roberts et al.*, 2014, and references therein]. The method uses minor hysteresis loops to calculate mathematical coercivity distributions and reversible and irreversible behavior of the magnetic carriers, and from such measurements to estimate single-domain (SD), pseudo-single domain (PSD), and multidomain (MD) contributions. Advanced FORC analysis has been developed to detect the presence of magnetofossils [*Egli et al.*, 2010], to roughly estimate,

without heating, the intensity of the external field in which thermoremanence was acquired [*Muxworthy and Heslop*, 2011] and for quantitative unmixing of magnetic components, primarily in sediments [*Heslop et al.*, 2014; *Lascu et al.*, 2015].

FORC distributions are calculated from measurements acquired almost entirely in fields several orders of magnitude larger than those found on the Earth's surface. Such fields can generate a large induced magnetic moment, particularly in rocks containing coexisting MD magnetic material. Strong induced signals create a practical challenge because they necessitate low instrumental sensitivity at the expense of precision in measurement of weak signals, including remanence. As FORC diagrams (and indeed the maps proposed in this work) are computed by calculating differences between adjacent reversal curves, when those differences are small yet the total signal is large, there is the possibility for cancelation or loss-of-significance errors, which reduce the resolution of such signals of interest. This contrast between strong induced signal and weak remanence may be pronounced in igneous and metamorphic rocks, particularly in coarse-grained samples that contain abundant and large discrete mixed oxide crystals.

Prior to the widespread adoption of FORC analysis, remanence-based techniques were used within the physics and geophysical disciplines [e.g., *Girke*, 1960; *Dunlop and West*, 1969; *Carvallo et al.*, 2005] that are a subset of the general family of second-order reversal curves (SORCs) [*Mayergoyz*, 1988; *Winklhofer et al.*, 2008] where the measurement field is not variable but, by definition, zero. Both SORC and FORC analyses can be used to calculate the Preisach distribution [*Preisach*, 1935] with similar results. Comparing simulated FORC and remanent SORC diagrams, *Stancu et al.* [2006] observe that the latter are less sensitive to reversible magnetization processes and magnetostatic interactions that are affected by the magnetic state of the sample in a strong field. While such information may be useful in the study of fundamental magnetization processes, they are of little value in characterizing remanence and low-field behavior.

A further widely applied and remanence-based characterization technique are isothermal remanent magnetization (IRM) acquisition curves. Using cumulative lognormal distributions, the contribution of one or more populations of magnetic carriers can be quantitatively measured [*Robertson and France*, 1994; *Stockhausen*, 1998]. *Egli* [2003] observes that the rescaling of applied fields from a linear to logarithmic scale effectively emphasizes weak high-coercivity signals with respect to low-coercivity carriers, the former of which are of greatest interest for paleomagnetic and fundamental magnetic studies. Remanence acquisition measurements are frequently used to calculate coercivity (of remanence, H_{cr}) distributions, but they lack direct information about magnetic interactions that can introduce distortions to the form of the distribution and lead to spurious inferences about intrinsic magnetic properties [*Egli*, 2003; *Heslop et al.*, 2004].

Here we describe a new measurement protocol that incorporates aspects of both FORC analysis and IRM acquisition curves in a remanent Preisach diagram acquired with logarithmic field steps. The use of a nonlinear field scale confers higher field resolution at small applied fields and greater sensitivity to changes in magnetization at large applied fields. Measuring in zero field avoids generation of large induced signals and increases sensitivity to remanence carriers by 1 – 3 orders of magnitude. This enables the detection of interaction fields within the sample that can hardly be observed with other techniques.

2. Remanent Magnetic Anomalies

The need for a remanent Preisach mapping technique was prompted by a suite of samples that generate remanent aeromagnetic anomalies in the Earth's field, but additionally contain abundant MD magnetic material that creates a strong induced signal in conventional in-field measurements. While remanence-dominated anomalies may be positive or negative (magnetic fields greater or less than the background generated by the surrounding crust), most of the samples used here originate from negative anomalies (magnetic lows), where we have documented that they arise from remanent magnetization [e.g., *McEnroe et al.*, 2009a] and provide a clear demonstration of the strength of the remanence signal in weak fields such as that at the Earth's surface. Negative anomalies are evidence both that the reversed natural remanent magnetization (NRM) is stronger than the magnetization induced in situ by the Earth's field and that there is a high-coercivity component that gives these samples magnetic stability on a geologic timescale. Common characterization methods use laboratory fields of up to 1 T, up to 5 orders of magnitude greater than those at the Earth's surface. Such fields saturate low-coercivity phases, whose magnetization may dominate the total moment and cause a loss of significance when trying to extract the much smaller contributions from high-coercivity minerals.
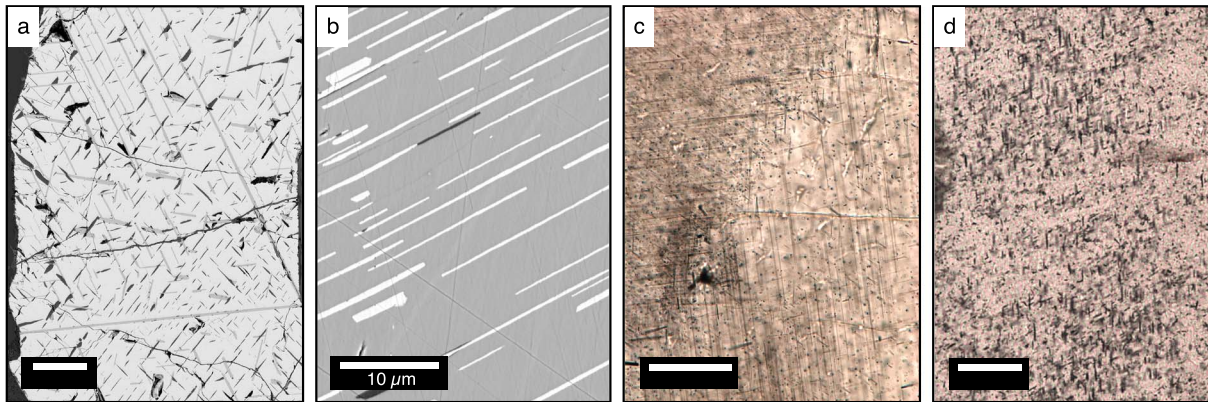
Figure 1. Remanence carriers in samples from the Mount Harcus, South Australia. Scale bars except for Figure 1b are 50 μm. (a) Backscattered electron (BSE) micrograph of coarse-grained magnetite (light gray), subdivided by ilmenite laths created by oxy-exsolution (medium gray) and magnesium-aluminum spinel lamellae created by spinodal decomposition (dark gray). (b) BSE image showing reduction exsolution of magnetite (light gray) and spinel (dark gray) in host ilmenite. (c) Acicular magnetite in plagioclase in plane-polarized light. The diagonal transition cutting the image is a crystallographic twin boundary that is highlighted by the change in orientation of the magnetite needles that form in defined crystallographic directions. (d) Acicular magnetite particles in pyroxene in plane-polarized light. Chemical analyses of the opaques in this phase is lacking, so additional phases may be present.

These high-coercivity phases, however, are commonly far more important than the dominating induced signal for paleomagnetic or rock magnetic interpretation, and samples such as these are a subject of ongoing interest for such applications [e.g., *Usui et al.*, 2015].

2.1. Mount Harcus Anomaly and Gabbroic Norite

To demonstrate the need for a highly dynamic and sensitive remanence mapping method, we apply several common magnetic characterization techniques to a complex sample from the Mount Harcus (South Australia) gabbroic norite. The sole magnetic carrier is magnetite that occurs in a variety of morphologies shown in Figure 1, which are predicted to have different domain states and coercivity ranges. These morphologies include discrete millimeter-size magnetite grains, which are subdivided by oxyexsolution of ilmenite lamellae and magnesium-aluminum spinel phases (Figure 1a). Some MD magnetite grains contain large ilmenite lamellae which themselves contain magnetite lamellae that are formed by reduction exsolution [*Robinson et al.*, 2016] (Figure 1b). Plagioclase and pyroxene contain acicular magnetite (Figures 1c and 1d). The discrete magnetite grains are predicted to be MD and have low coercivity and remanence, but due to their large volume also have a large induced magnetization even in weak laboratory fields. The smaller magnetite laths in ilmenite and the acicular magnetite in the silicates are more likely to be SD and have a higher coercivity and remanent magnetization but are volumetrically less abundant. The Mount Harcus intrusion is the source of a strong negative aeromagnetic anomaly, and the average NRM of over 550 specimens from six boreholes is 29 A/m [*Austin et al.*, 2014], an order of magnitude greater than typical igneous specimens [*Dunlop and Özdemir*, 1997].

Figure 2 contains results of several widely used magnetic characterization techniques applied to Har7 426.5 from the Mount Harcus norite. Measurements of bulk coercivity, such as the hysteresis loop shown in Figure 2a, are dominated by the volumetrically abundant, low-coercivity, MD magnetite; the stable carrier that generates the remanent aeromagnetic anomaly cannot be distinguished. Furthermore, the use of in-field bulk magnetic parameters in multivariate trend plots such as the Day plot [*Day et al.*, 1977] can be misleading (Figure 2b). The Mount Harcus samples contain potentially multiple distributions of both MD and SD particles and consistently plot between the SD-MD and SD-superparamagnetic (SP) mixing lines calculated by *Dunlop* [2002], in a region that is characteristic of bimodal SD-MD mixtures. The same area of the plot has also been described by *Kumari et al.* [2015] as characteristic of mixtures of SD grains and SP ferrofluid, confirming the poor interpretational value of bulk magnetic parameters.

The FORC diagram in Figure 2c is presented in Preisach H_a and H_b coordinates (see below), with the rotated FORC coordinate system H_u and H_c also indicated. The strongest signal is that with contours parallel to the H_u axis and coercivities here below 30 mT: these plot the irreversible magnetization changes (i.e., Barkhausen jumps) in the MD magnetite [*Pike et al.*, 2001]. The color scale for all figures in this work is full range, which here demonstrates the relative strength of the MD signal compared to all other irreversible signals. Figure 2c
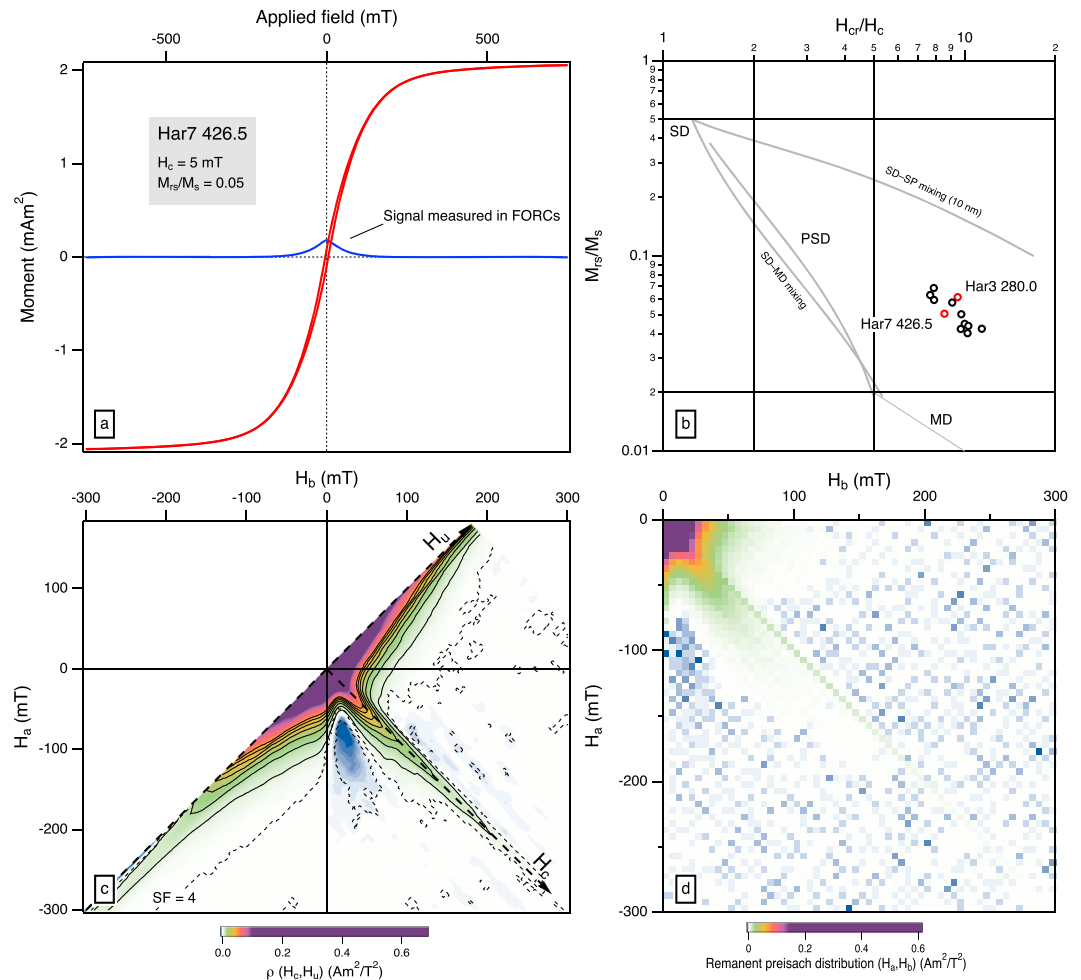
Figure 2. Conventional rock magnetic measurements of sample Har7 426.5 from the Mount Harcus gabbro-norite. (a) Hysteresis loops of these samples are dominated by low-coercivity, high-magnetization component, and the stability implied by the aeromagnetic anomaly associated by the intrusion is masked. (b) Samples plot consistently in a region of the *Day et al.* [1977] plot associated with mixtures of grain size and domain state above the SD-MD mixing curve calculated by *Dunlop* [2002]. (c) FORC distribution is dominated by a strong MD signal parallel to the H_u axis, although the signal along the H_c diagonal indicates the presence of noninteracting SD carriers. (d) A linear remanent Preisach distribution shows that most of the IRM is controlled by low-coercivity carriers, but the signal along the diagonal extending to 200 mT indicates the additional contribution of a high-coercivity component.

also shows an SD ridge extending along the H_c axis beyond 200 mT, which asymmetrically spreads off the axis with stronger signal below it than above. While the asymmetry is reproducible in other analyses, at high H_c values the true SD ridge should be an infinitely fine feature: its spread in the FORC diagram is at least partially due to the data smoothing required to resolve its signal, which is weak compared to that of the MD in an in-field analysis. The hysteresis loop in Figure 2a illustrates that the irreversible signal used to calculate the FORC distribution of this sample is less than 10% of the total instrument range required for this measurement, which enhances the risk of loss-of-significance errors and necessitates smoothing for weak moments.

Like FORC diagrams, remanent Preisach distributions are homogeneously sampled through regular field intervals in most cases [e.g., *Daniel and Levine*, 1960]. Unlike FORCs, Preisach diagrams are only sensitive to processes that affect magnetic remanence, being therefore associable with some form of H_{cr} distributions. Other reversible or irreversible magnetization changes captured by FORC diagrams are automatically excluded from the Preisach space. The trade-off of the lack of data relating to processes occurring where $H \neq 0$ is greater resolution of weak signals, due to the fact that only moments up to M_{rs} are measured rather than M_s as for FORCs. Comparison of the remanent Preisach diagram in Figure 2d with the FORC of the same sample shows that within the measurement space that they share, the irreversible distribution of the two techniques records the

same features, both positive and negative. Some features, such as the SD ridge along the diagonal line from upper left to bottom right of the Preisach diagram, are more distinct due to lack of data smoothing. However, sampling at regular field intervals has disadvantages, particularly in remanence. Most of the H_{cr} distribution is found near $H_a, H_b = 0$, with coercivity values less than 25 mT. This region is poorly sampled, with only a few data points describing a large proportion of the total remanence. The inability to finely resolve phenomena responsible for this remanence, including important domain wall processes, is one of the primary criticisms of remanent Preisach diagrams leveled by *Carvallo et al.* [2005] in their comparison with FORC analysis. Because the measurement of remanence is time-consuming, it is impractical to measure equidistantly sampled remanent Preisach diagrams on samples with a wide range of coercivities at finer resolutions than shown here (5 mT steps, requiring about 9 h for 3600 data points or more than 3 times the time required for the FORCs of the same sampling resolution). A solution is needed that balances the time limitations of fine sampling at low coercivities with the need to reach high fields to resolve high-coercivity signals.

2.2. Remanent Anomalies Associated With Lamellar Magnetism

While single-phase hematite is much less magnetic than magnetite and ilmenite is paramagnetic at room temperature, the nanoscale intergrowth of these phases gives rise to lamellar magnetism, which has been identified as the source of strong remanent aeromagnetic anomalies [e.g., *McEnroe and Brown*, 2000; *McEnroe et al.*, 2001a, 2001b; *Kasama et al.*, 2004; *McEnroe et al.*, 2004a; *McCammon et al.*, 2009; *McEnroe et al.*, 2009b]. Lamellar magnetism is the enhancement of magnetization at the interface between the phases caused by the accommodation of differing crystal structures [*Robinson et al.*, 2002, 2004; *Robinson*, 2006; *Harrison*, 2006; *Pentcheva and Nabi*, 2008; *Kasama et al.*, 2009; *Brok et al.*, 2014]. The resulting cation and magnetic spin ordering create a strong ferrimagnetic signal with high coercivity.

The samples exhibiting lamellar magnetism presented in this study are all associated with strong negative aeromagnetic anomalies and have a variety of ilmenite-hematite intergrowth morphologies. Samples from two localities contain exclusively rhombohedral oxides, and two also contain coexisting magnetite. Of those containing only rhombohedral oxides, samples 004–3 (Rogaland, Norway) and AL7b (Allard Lake, Quebec) both contain abundant ilmenite-hosted hematite lamellae with varying amounts of second-generation hematite lamellae with ilmenite exsolution. Sample 004–3 is a hemo-ilmenite ore composed primarily of ilmenite which contains precipitates of titanohematite ranging in size from the nanoscale up to a thickness of approximately 3 μm [*McEnroe et al.*, 2002]. AL7b is also a hemo-ilmenite ore that in addition contains large (≈40 μm thick) titanohematite lamellae that host nanoscale ilmenite precipitates [*McEnroe et al.*, 2007; *Robinson et al.*, 2013]. Light and electron microscopy, magnetic characterization, and Mössbauer spectroscopy [*Dyar et al.*, 2004; *Frandsen et al.*, 2007] confirm that these samples contain no magnetite.

The remaining samples are more complex and contain both ilmenite-hematite intergrowths and abundant coexisting MD magnetite, with NRM much greater than magnetization induced in the crust. OSW1–2 is a granulite-grade microcline gneiss from the Oswegatchie region of the Adirondack mountains associated with a strong negative remanent anomaly [*Balsley and Buddington*, 1958; *McEnroe and Brown*, 2000]. It contains magnetite in concentrations of ≈3% and nanometer- to micrometer-scale ilmenite precipitates within hematite and is unique among these samples as it contains little to no hematite precipitates within the ilmenite [*Brown and McEnroe*, 2012]. Sample S11–8 is from a granulite-facies meta-gabbro from southwest Sweden and contains the most varied magnetic mineralogy, with nanometer- to micrometer-scale hematite-hosted ilmenite and ilmenite-hosted hematite, and coexisting magnetite in grains measuring 50–200 μm [*McEnroe et al.*, 2001b]. In both cases, the MD magnetite creates a large induced magnetization which is the dominant signal measured during laboratory in-field techniques, limiting the utility of such methods in characterizing the high-coercivity remanence carriers.

3. Theoretical Background of Preisach Diagrams

The first description of hysteresis processes as the sum of elemental contributions of squared hysteresis loops called hysterons was given by *Preisach* [1935], after discussions with Prof. R. Becker, who also outlined it in one of the first modern textbooks on ferromagnetism [*Becker and Döring*, 1939]. The theory was initially proposed as purely a mathematical construct for magnetization processes in multidomain materials, in which hysterons do not have a direct physical meaning. A modified version of this model was later applied to rock magnetism by *Néel* [1944], who first interpreted the purely mathematical model in terms of shifted single-domain particle loops. Since then Preisach mapping has been used in material science [*Girke*, 1960; *Della Torre*, 1966] and
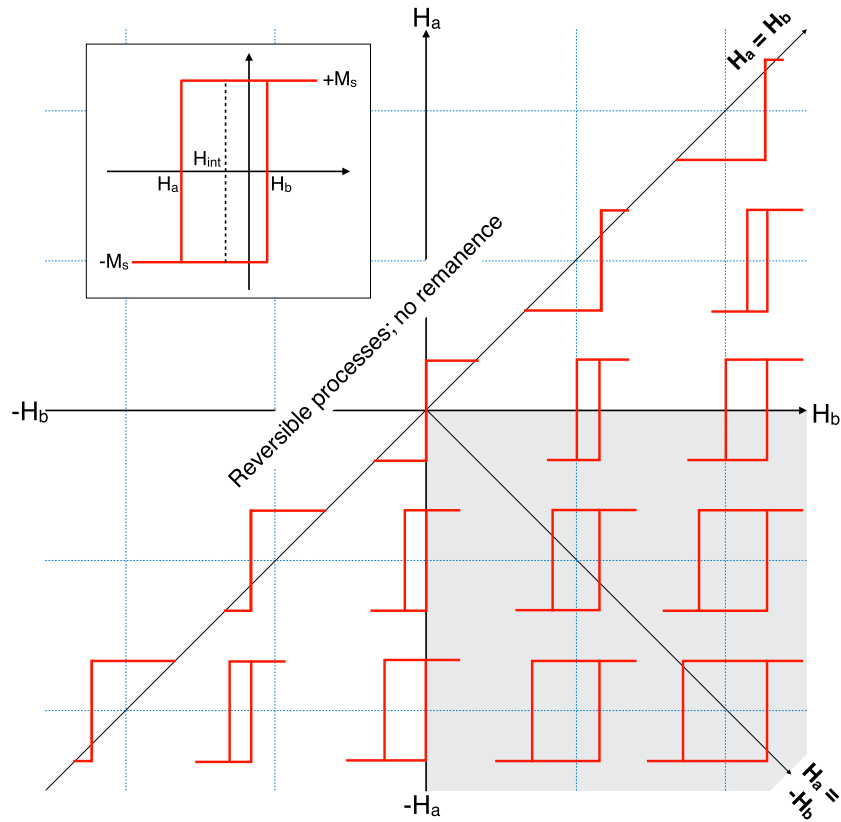
Figure 3. (inset) Hysteron with switching fields H_a and H_b, offset by interaction field H_{int}. (main) Preisach hysterons and their distribution as function of H_a, H_b. Unbiased hysterons lie upon the $H_a = -H_b$ diagonal and biasing fields H_{int} increase with distance perpendicular to $H_a = -H_b$. Preisach theory also includes descriptions of reversible processes, but they are not applicable in the present discussion and are not depicted. After *Fabian and von Dobeneck* [1997].

geophysics [*Dunlop and West*, 1969; *Ivanov et al.*, 1981; *Zelinka et al.*, 1987; *Hejda and Zelinka*, 1990; *Dunlop et al.*, 1990], but only with the advent of fast vibrating sample magnetometers (VSMs), a standard measurement scheme (FORC) has been established [*Pike et al.*, 1999] and widely applied and analyzed [*Roberts et al.*, 2014].

Preisach theory describes hysteretic processes in terms of the sum of elemental rectangular hysterons characterized by two fields, H_a and H_b at which the magnetization is switched from positive to negative saturation (H_a) and vice versa (H_b) (Figure 3, inset). These hysterons can be represented in a two-dimensional half-space whose Cartesian coordinates are given by H_b and H_a with $H_b \geq H_a$ (Figure 3). In this half-space one can distinguish several cases: symmetric hysterons are characterized by $H_a = -H_b$ and lie upon the corresponding diagonal. A physical realization of such hysterons might be given by isolated SD particles. The values of H_a and H_b may also be unequal, in which case the hysteron is shifted by some value. In the spirit of Néel's interpretation this shift is referred to as the interaction field H_{int}, because he attributed this bias to magnetostatic interactions between discrete particles. In a more general sense, bias can reflect a multitude of other switching phenomena, including response to internal fields.

The magnetic behavior of a macroscopic magnetic sample, such as a rock, is the sum of the switching of a large number of hysterons with varying values of H_a and H_b. It can be represented by a distribution function $p(H_a, H_b)$ of hysterons with given H_a and H_b values. The distribution $p(H_a, H_b)$ is characteristic of a sample and may be used to infer information about both the intrinsic properties of magnetic carriers and their interaction with their local environment. Accordingly, the total sample magnetization is modeled by the integral

$$M = \int_{S^+} p(H_a, H_b)\, dH_a\, dH_b - \int_{S^-} p(H_a, H_b)\, dH_a\, dH_b, \qquad (1)$$

where $S^\pm$ are the areas in the $H_a - H_b$ plane where the hysterons are in positive/negative magnetization state [e.g., *Hejda et al.*, 1994].

Zero-coercivity hysterons along the $H_a = H_b$ diagonal represent reversible magnetization processes. Hysterons above this diagonal, on the other hand, would be characterized by inverted ascending and descending branches that violate the first principle of thermodynamics. Only hysterons in the fourth quadrant of the (H_a, H_b) space, i.e., those with switching fields of opposed sign (shaded area in Figure 3), are important for the description of remanent magnetizations, as these are the only hysterons that would not have always the same positive or negative saturation state in zero field. Statistically, in remanence the distribution function $p(H_a, H_b)$ in the regions below the $H_a = H_b$ diagonal and outside the fourth quadrant will typically be equal $(p(H_a, H_b) = p(-H_b, H_a))$ and their oppositely signed integrals in (1) will sum to zero. These areas may not sum to zero in the presence of an applied field, so FORC diagrams include the entire $H_a \leq H_b$ half plane, usually in a rotated (H_c, H_u) coordinate system.

The region containing the hysterons responsible for measurable remanent behavior is therefore the region $H_a \leq 0, H_b \geq 0$, and figures in this work will include this area solely. Physical relations between remanent and induced magnetization curves and magnetization parameters of natural samples can be analyzed mathematically by means of Preisach theory [*Fabian and von Dobeneck*, 1997]. Qualitatively, features in various regions of the Preisach diagram can be used to infer information about coercivity and switching behavior of the magnetic carriers. Because the diagonal $H_a = -H_b$ corresponds to symmetrical hysterons, signal along this line can be interpreted as particles obeying *Stoner and Wohlfarth* [1948] reversal mechanisms; in the context of rock magnetism, such a signal measures the contribution of SD particles. Here the $H_a = -H_b$ line of the Preisach diagram will be referred to simply as "the diagonal." Signal off the diagonal indicates influence of interaction fields resulting in biasing of the hysterons: in rock magnetism this may indicate strong magnetostatic or exchange interactions between separate particles. In pseudo-single domain (PSD) or multidomain carriers, off-diagonal signals result from the spontaneous response (including vortex or domain wall nucleation, translation, and annihilation) to demagnetizing and local interaction fields.

4. Experimental Methods

4.1. Mapping Remanent Magnetization

The measurements presented in this work were performed on a Princeton Measurements Corp. MicroMag 2800 VSM at ≈25°C. The acquisition protocol is similar to that applied by *Bate* [1962] and also analogous to that of FORCs:

1. Create unique initial $+M_{rs}$ state by applying and removing a maximal positive field.
2. For $i = 1, \ldots, N$ apply and remove the negative *conditioning field* $H_a = -H_i$.
3. Stepwise apply and remove the positive *back fields* $H_b = +H_j$ for $j = 1, \ldots, N$.
4. For each combination of i and j measure resulting remanence $M_r(-H_i, +H_j) = M_r(H_a, H_b)$.
5. Increase i and continue with step 2.

The complete Preisach map consists of a series of individual remanence curves, with sampling steps $H_1, \ldots, H_N$ for the H_a and H_b sequence of fields determined by the magnetometer software, which uses an approximation of the hyperbolic sine function. For example, in Figure 5a within instrumental constraints we used the sequence

$$H_i = \alpha \, \sinh\left(\frac{i}{\beta}\right), \alpha \approx 0.002 \, \text{mT}, \beta \approx 15 \tag{2}$$

The resulting sampling scheme can be visualized on a linear scale in Figure 4. This work presents Preisach maps that were acquired with varying values of α and β.

Within instrumental constraints, the sequence H_i of measurement fields can be chosen freely, and it might be optimal for each sample to first measure an IRM acquisition curve, and only afterward to choose an optimized field sequence H_i that gives equidistant magnetization steps IRM(H_i) for $i = 1, \ldots, N$, similar to the sampling scheme for FORCs implemented by *Zhao et al.* [2015]. We did not implement this approach because approximately logarithmic field steps are almost equally efficient and conceptually simpler. In addition, for some samples equidistant magnetization sampling can yield extremely distorted field sequences which are not guaranteed to give an optimal representation of the Preisach function.

The Preisach remanence map acquisition with the VSM is automated using a script for the Windows automation software AutoIt (code available from the authors on request). Measurement time is primarily a function
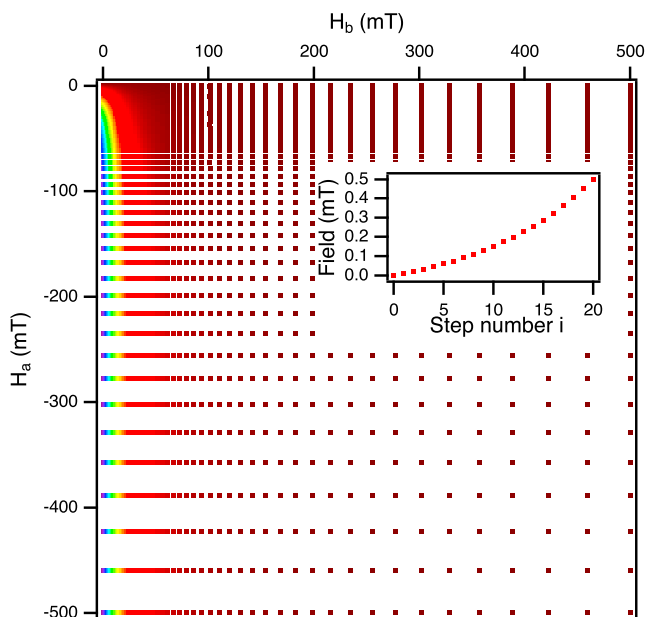
Figure 4. Distribution of measurement fields using logarithmic sampling. The scheme provides dense sampling at low coercivities and wide field steps at high, which enhances sensitivity to small rates of change in magnetization. Color scale is magnetization data that produce remanence map presented in Figure 5a. (inset) Field steps at smallest fields.

of number of data points as the magnetometer electromagnets must be ramped up and down between each point, and there is also a lesser dependence on the maximum field applied. Using moderate averaging times of 1–2 s per point, the acquisition of a complete remanence map takes between 5 h for a 40×40 matrix and 24 h for the 100×100 data sets presented in this work. While considerably longer than the acquisition of a similar number of data points using the FORC method, the recommended practice of averaging multiple FORC measurements to attain sensitivity to weak components can also require many hours to days to produce high-quality data [*Egli et al.*, 2010; *Roberts et al.*, 2014]. In order to improve signal-to-noise ratio of weak samples and improve the statistical significance of results, large specimens of up to 4 g were glued directly to the VSM sample holder for measurement.

4.2. Generation of Nonlinear Preisach Maps

The remanent Preisach maps presented in this work are based on nonlinear field sampling at nonequidistant field steps H_i, to achieve an appropriate sensitivity at all different applied field intensities. The maps plot the change $\Delta M_r(H_a, H_b)$ in remanent magnetization in a rectangular field region delimited by four pairs of conditioning and backfield around (H_a, H_b): (H_{i-1}, H_{j-1}), (H_{i-1}, H_j), (H_i, H_{j-1}), (H_i, H_j), following *Daniel and Levine* [1960]:

$$\Delta M_r(H_a, H_b) = (M_r(H_i, H_j) + M_r(H_{i-1}, H_{j-1}))$$
$$- (M_r(H_i, H_{j-1}) + M_r(H_{i-1}, H_j)). \quad (3)$$

Note that by this definition the remanent Preisach map does not approximate the Preisach density function $p(H_a, H_b)$, because the magnetization change is not divided by the area $(H_i - H_{i-1}) \times (H_j - H_{j-1})$. This means that the remanent Preisach map does not plot the magnetization density or the change in magnetization per regular field step—as do FORC distributions and linearly sampled Preisach diagrams—but the total magnetization change in each of the differently sized rectangles. The nonlinear sampling scheme therefore not only serves to measure the remanence map in a time-efficient fashion, but also improves signal-to-noise at high coercivities (where the sampling steps are large, which compensates for the relatively small rates of change in magnetization). Unlike FORC distributions, the remanent Preisach maps require no smoothing due both to the smaller number of data points and this enhanced sensitivity at high fields. This avoids introducing artifacts, such as broadening of fine features in smoothed FORC diagrams [*Heslop and Muxworthy*, 2005; *Harrison and Feinberg*, 2008; *Egli*, 2013]. (A method to calculate the Preisach density as a function of $\log H_{a,b}$ is presented in Appendix A. This processing yields Preisach maps that are qualitatively identical to the raw magnetization maps but can be more rigorously compared with other techniques; for ease of comprehension we present the raw magnetization here.)

Various parameters that aid the comparison or interpretation of remanence maps can be calculated from the Preisach map or extracted directly from the IRM data. All of the remanence maps here include a graph of a calculated IRM acquisition curve $M^*_{IRM}(H)$, as well as lines that indicate the area of the Preisach map which

contains a given proportion of this calculated IRM. $M^*_{IRM}(H)$ is calculated from the Preisach density $p(H_a, H_b)$ by integration:

$$M^*_{IRM}(H) = \int_{\substack{H_a \geq -H \\ H_b \leq H}} p(H_a, H_b)\, dH_a\, dH_b. \tag{4}$$

In case of a stable symmetric Preisach function, $M^*_{IRM}(H)$ coincides with a real IRM curve measured from an initially AF demagnetized state [*Fabian and von Dobeneck*, 1997]. The percentage lines are then directly calculated from this $M^*_{IRM}(H)$ curve. These lines illustrate discrete parts of the diagram, such as high-coercivity phases, that are solely responsible for some proportion of the total magnetic signal. In describing maximum and minimum coercivities in this work, we will generally refer to components that control remanence within the 10th–90th percentiles.

The integration involved in (4) becomes simply a summation over the magnetization of the remanent Preisach map:

$$M^*_{IRM}(H) = \sum_{\substack{H_a \geq -H \\ H_b \leq H}} \Delta M_r(H_a, H_b) \tag{5}$$

Direct summing of the magnetization from discrete regions of the diagram is an advantage of using the absolute magnetization in the remanence map rather than a smoothed distribution, where accuracy and precision very much depend on the details of the calculation used to obtain the Preisach distribution. Such calculations can also be used to measure the contribution of characteristic magnetic phases (such as SD particles or bulk hematite) to the total IRM response.

A final calculation useful for interpreting remanence maps are contours of equal offset perpendicular to the diagonal. In Preisach theory, such an offset indicates biasing of the hysterons, which may result from magnetostatic interactions, although in most of the cases presented here result from the action of the demagnetizing fields in MD particles. As these interaction contours are parallel to the diagonal in linearly sampled Preisach diagrams, in remanence maps they serve as guides to eye that illustrate the distortion introduced by the log-log sampling and display of the Preisach map, which imparts or accentuates a teardrop shape in distributions that would otherwise have a more regular form. They also demonstrate that this sampling scheme does not resolve small shifts off the diagonal for hysterons with high coercivity.

5. Applications

5.1. Magnetite Standards

To observe ideal magnetic behavior and inform interpretation of more complex mineralogies, we measure two well-characterized magnetite standards using the remanent mapping technique. Figure 5a is a map of the Tiva Canyon Tuff standard provided by the Institute for Rock Magnetism at the University of Minnesota (specimen TC05_9 #6), which is predominantly SD with a small superparamagnetic (SP) component [e.g., *Worm and Jackson*, 1999]. Figure 5b is a Preisach map of synthetic magnetite particles from Wright Industries (W6) with mean size 12.1 μm [*Krasa et al.*, 2003], likely above the MD threshold for this material although potentially containing some PSD component.

The remanence map for the Tiva Canyon Tuff (5a) is dominated by ridge along the diagonal, which corresponds to the central ridge in FORC diagrams. This ridge is a typical signature of noninteracting SD particles [*Newell*, 2005; *Egli et al.*, 2010]. Less than 5% of the IRM is acquired below 10 mT. Frequency-dependent magnetic susceptibility [*Worm and Jackson*, 1999] clearly shows abundant SP particles in this sample, providing evidence for a magnetite particle size distribution covering SP and SD grain sizes from at least 5–50 nm. Transmission electron micrographs (TEM) by *Schlinger et al.* [1991] indicate that the grain size distribution is unimodal. Based on these observations the well-defined lower end of the coercivity spectrum above 10 mT apparently shows that coercivities between 0 mT and 10 mT are statistically unlikely for magnetite in the single-domain range, at least using remanence measurement on timescales of the order of 1 s. As predicted for a uniform size distribution of SD magnetite, the coercivity distribution is narrow, between 20 and 70 mT representing the 10th–90th percentiles of magnetization, reaching saturation by 100 mT. The sharp upper end is due to the material properties of magnetite which limit the maximal coercivity because grains above the SD-vortex threshold size ($\approx$50–80 nm for near-equidimensional particles) have a dramatically lower coercivity and may contribute to the very slight spreading off the diagonal. The TEM studies indicate that the
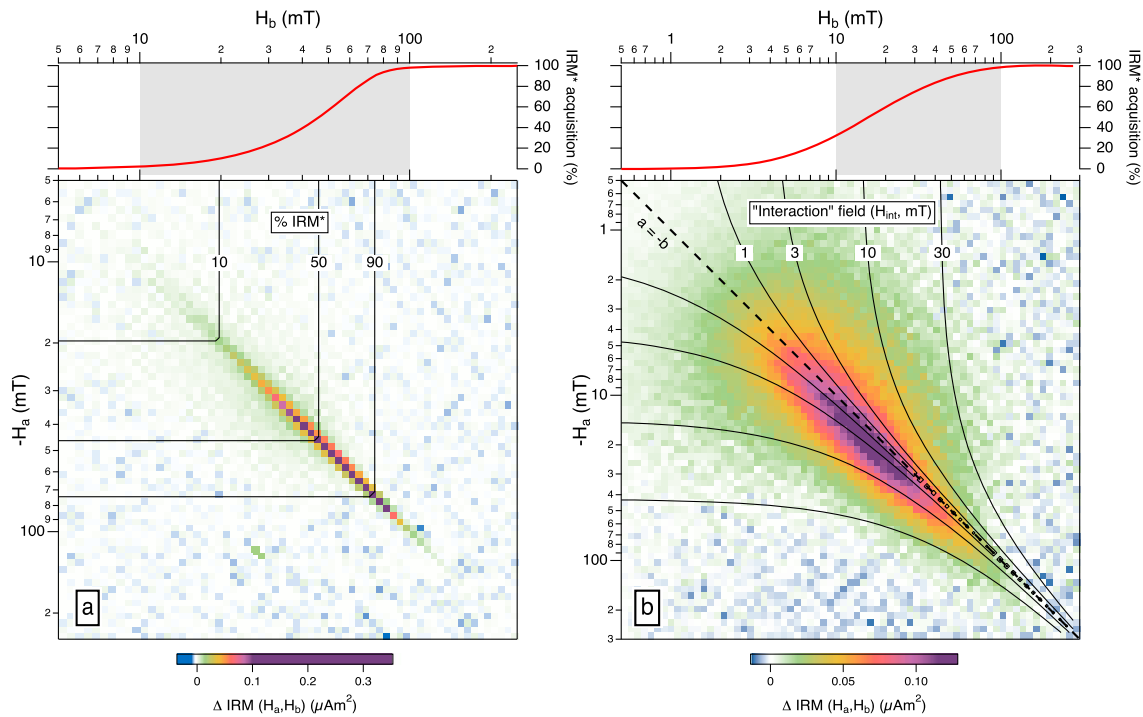
Figure 5. Nonlinear remanence maps illustrating typical features of the technique. Shaded box in every IRM acquisition graph in this work is a guide to the eye to indicate the coercivity range 10–100 mT, and to aid comparison between maps with different field ranges. (a) Tiva Canyon Tuff SP-SD magnetite standard. Signal directly along the diagonal is model SD behavior. (b) Synthetic magnetite with mean particle size 12.1 μm (Wright Industries W6) shows spreading perpendicular to the diagonal, indicative of internal fields biasing the hysterons that comprise the distribution, the strength of which is indicated by the curved contours.

magnetite grains can be closely spaced, such that magnetostatic interaction may be an alternate explanation for the slight off-diagonal spreading of coercivities. The signal off the diagonal appears stronger above rather than below $H_a = -H_b$.

The Wright magnetite sample analyzed in Figure 5b shows a much wider range of coercivities than the SD sample, with $M^*_{IRM}(H)$ indicating that more than 50% of the remanence is held by particles with coercivities less than 20 mT. Similar to Figure 5a, for this sample with a nominal grain size of 12.1 μm the sample saturates by 100 mT. The peak of the distribution in Figure 5b is offset below the diagonal caused by the highly asymmetric measurement protocol. In spite of the overall downward shift, the spread of the distribution is slightly more pronounced above the diagonal $H_a = -H_b$, similar to the SD-PSD spread in Figure 5a.

The most prominent feature of MD magnetite is the spreading of the distribution off the diagonal, in this case indicating the action of the demagnetizing field in creating asymmetric switching behavior. The strength of this biasing effect can be directly measured using the "interaction" contours shown in Figure 5b, which imply that the effect is generally below 30 mT. The interaction contours serve as visual aids and demonstrate that the resolution of the off-diagonal shift is proportional to the applied field, which allows precise determination of small shifts off the diagonal for hysterons with low coercivity but limits resolution for high fields. While this limited resolution is a disadvantage of nonlinear sampling, the accuracy of small field differences at high-field values is nonetheless reduced regardless of sampling scheme. Therefore, equidistant schemes that spend a large fraction of their measurement time at high fields while neglecting the much more accurately measurable and physically important low-field region are arguably not the most time-efficient approach.

5.2. Magnetite-Dominated Rocks

The application of remanence mapping to rocks with complex magnetic mineralogy allows the identification of multiple remanence carriers with higher sensitivity and finer resolution of processes at low coercive fields. The different magnetite morphologies in the Mount Harcus gabbroic norites presented in Figure 1 are predicted to have a range of domain states and hence magnetic properties, and the remanent Preisach maps of Figure 6 contain features with similarities to the near-ideal behaviors described in Figure 5.
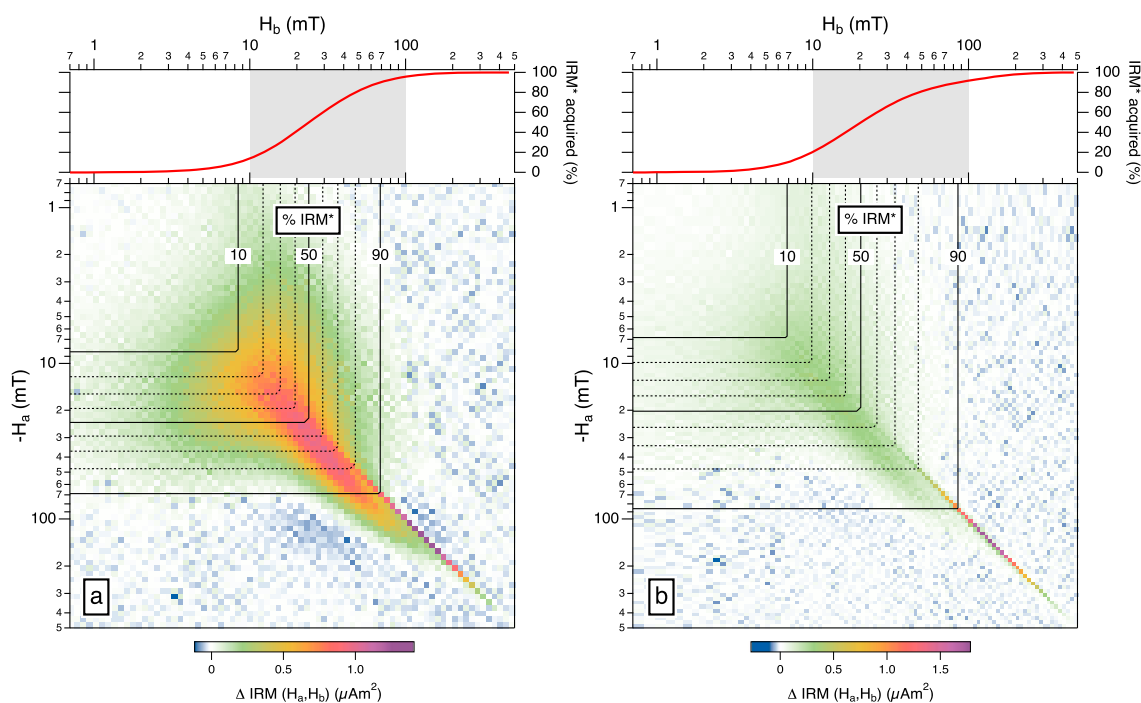
Figure 6. Nonlinear Preisach diagrams of samples from Mount Harcus. (a) Har7 426.5. Two distinct magnetic behaviors can be observed: a distribution centered around 30 mT offset below the diagonal and spread both parallel and perpendicular to it, and a high-coercivity distribution along the diagonal above $\approx$60 mT. More than 90% of the remanence is carried by the low-coercivity distribution. (b) Har3 280.0. Both distributions are present although the intensity of the low-coercivity phase is reduced. Around 50 mT it can be seen that the low-coercivity distribution is offset from the diagonal, while the high-coercivity distribution is not.

The Preisach map shown in Figure 6a (sample Har7-426.5) is the same as that which yielded the FORC diagram and linear Preisach distribution presented in Figures 2c and 2d, respectively. The strongest signals in the FORC and linear Preisach diagrams are low-coercivity signals near the origin. In FORC diagram, this low-coercivity signal creates contours parallel to the rotated FORC H_u axis and is diagnostic of the abundant MD magnetite. A similar strong signal can be observed near the origin of the linear Preisach distribution, although due to the reduced measurement space, it does not have the same diagnostic ability. Both distributions also contain signal along the diagonal (equivalent to the rotated FORC axis H_c in Figure 2c), representing noninteracting SD particles. There is also a spread off the diagonal, which makes the central ridge of the FORC diagram appear asymmetric, while in the linear Preisach distribution there is a diffuse signal below and visibly offset from the diagonal. There is also a negative region around $H_a \geq -150$mT, $H_b \leq 50$ mT.

The nonlinear Preisach map of the same sample in Figure 6a contains many of the same features, with some important differences. The dominant low-coercivity signal in Figures 2c and 2d is deemphasized by the logarithmic sampling and plotting of the raw magnetization, and the distribution shows very little signal below $\approx$3 mT. Between $\approx$5 and 60 mT, the distribution is widely spread perpendicular to the diagonal, similar to the Wright magnetite standard distribution discussed in Figure 5b. At coercivities above $\approx$60 mT, the spread is less pronounced and is offset below the diagonal, similar to the asymmetry seen in Figures 2c and 2d. There is also a strong signal at high coercivities along the diagonal, the intensity of which is emphasized by the relatively coarse sampling spacing in this part of the diagram and the plotting of absolute magnetization. The negative signal present in both the FORC and linear Preisach diagrams is present below the diagonal in a similar coercivity range $-H_a \leq 200$ mT, $H_b \leq 50$ mT.

The same features are present in Figure 6b (sample Har3 280.0) although the relative strength of the components vary. The lowest-coercivity signal (<20 mT) is similarly spread perpendicular to—and offset below —the diagonal. The stronger signal in Har3 280.0 is the high-coercivity distribution lying along the diagonal, which at its low-coercivity end ($\approx$30–80 mT), is clearly distinct from the broad and offset signal described above. This signal is more clearly separated and persists to higher coercivities in Figure 6b. The separation of these two signals on the remanence map is a clear advantage of the technique over IRM curve unmixing:

Table 1. Proportion of Total IRM Calculated From Discrete Regions of the Remanent Preisach Map[a]

	Magnetite Carrier		Multiphase Carriers			
	Har3 280.0	Har7 426.5	OSW1−2	004−3	AL7b	S11−8
Total IRM (μA m^2)	217	334	11	70	34	86
Magnetite with interactions (%)	92	97	52			68
Noninteracting magnetite (%)	8	3				
Noninteracting hematite in ilmenite (%)				36	16	4
Offset hematite trough (%)			45	64	84	26
(Negative peak) (%)			−9	−7	−9	−8

[a]Percentages do not always sum to 100 due to rounding and overlapping signals.

while these two phases can be inferred from single IRM curves and fit using cumulative log Gaussian distributions (Har3 280.0 more robustly than Har7 426.5), the remanence map indicates that these phases not only have distinct microcoercivity distributions, they also are subjected to very different magnetization processes.

The $M^*_{IRM}(H)$ curves and the related percentage lines indicate that the distribution along the diagonal accounts for somewhat less than 10% of the total IRM; its contribution can be precisely calculated by summing the data points in the remanence map according to equation (5). The calculations presented in Table 1 indicate that the SD signal of Har3 280.0 (Figure 6b) accounts for 8% of the total IRM, as compared to 3% of Har7 426.5. The variation in proportion of SD carriers is consistent with NRM values, 56 A/m for Har3 280.0, compared to 24 A/m for Har7 426.5, despite the latter having a higher magnetite content.

The difference in intensity of the low-coercivity, interacting distribution compared to that of the high-coercivity, noninteracting signal in these two samples results from the varying ratio of the contribution of the respective distributions. Following the discussion of *Egli* [2003], resampling of the remanence map on a non log$_{10}$ scale for display purposes could be employed to enhance low- or high-coercivity features with respect to the rest of the graph.

5.3. Multiphase Carriers

The unique magnetic properties of hematite-ilmenite intergrowths and resulting lamellar magnetism generate signatures in remanence maps that allow them to be distinguished from magnetite. These signatures are useful for identifying their presence and are a fingerprint of types of microstructure and provide information about fundamental magnetization processes in the rhombohedral oxides.

Sample OSW1−2 contains magnetite and titanohematite with ilmenite exsolution [*Brown and McEnroe*, 2012], and both carriers can be identified in the remanence map displayed in Figure 7a and in the $M^*_{IRM}(H)$ curve. The magnetite distribution, qualitatively similar to that shown in Figure 5b but faintly visible due to the relative strength of the high-coercivity component, is spread off the diagonal and accounts for approximately 50% of the total IRM. The $M^*_{IRM}(H)$ curve and spacing of the remanence contours indicate that the remaining remanence is held by a second phase with a coercivity over 150 mT, in agreement with the alternating field demagnetization presented by *Brown and McEnroe* [2012] (Figure 10, sample AD6-2-2B). In the Preisach diagram this remanence is controlled by a feature that is an elongated peak offset below the diagonal. There is also a weak negative trough associated with this peak, further offset below the diagonal and below the elongated peak. The possible origin of such negative troughs for SD ensembles has been discussed by *Newell* [2005].

The FORC diagram of the same specimen in Figure 7b contains many of the same features as the remanence map, but illustrates the challenge of examining remanence carriers in the presence of abundant MD material. The dominant signal is the low-coercivity distribution parallel to the H_u axis generated by the MD magnetite, and measures the irreversible magnetization changes (Barkhausen jumps) along the major hysteresis loop. The high-coercivity remanence carrier is nearly an order of magnitude weaker and consequently noisy. While the dashed significance contours indicate that the FORC measurement is capable of measuring this peak, the disproportionate strength of the MD signal in the in-field measurement requires substantial smoothing that risks distorting fine features. Such distortion will only be exacerbated by existing implementations of variable smoothing, such as the otherwise successful VARIFORC processing [*Egli*, 2013], which are optimized to preserve features along and symmetrical about the central ridge.
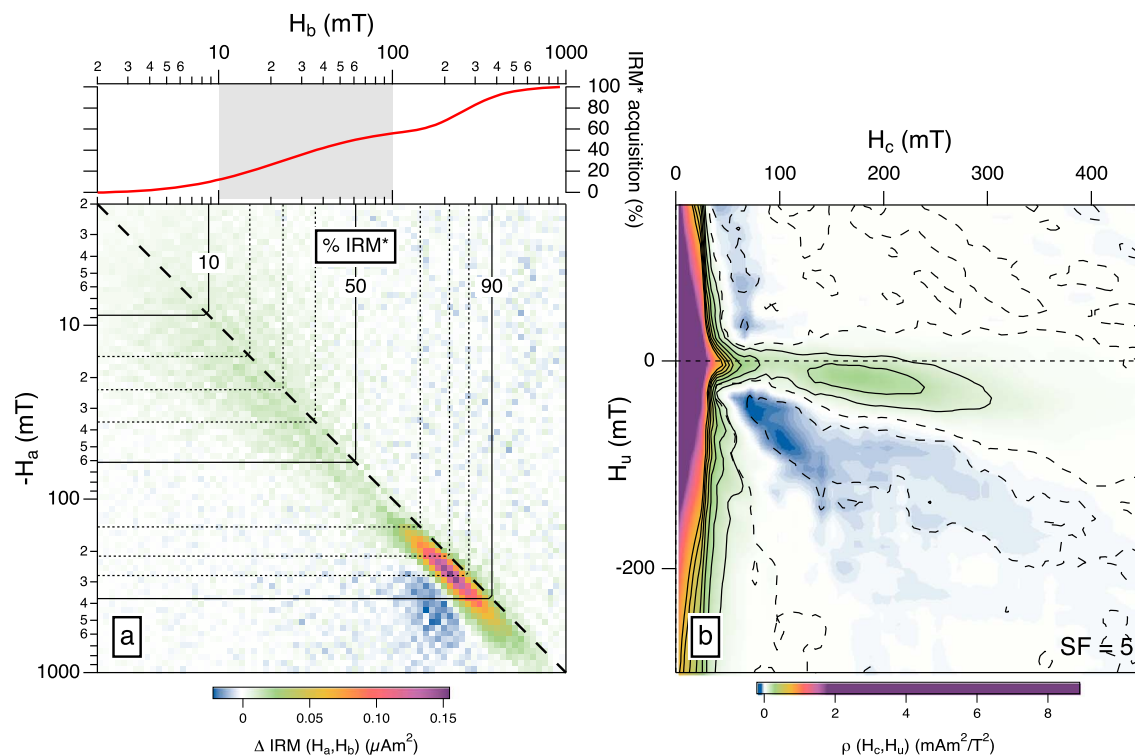
Figure 7. OSW1–2 gneiss containing titanohematite and coexisting magnetite. (a) Preisach diagram indicates that approximately 50% of remanence is carried by low-coercivity phases. The remaining remanence results from high-coercivity titanohematite that generates characteristic offset peak located below the diagonal. (b) FORC diagram of the same specimen illustrates both the strength of induced magnetization (the large signal with $H_c > 25$ mT) and the same offset high-coercivity peak. The logarithmic scaling of the axes in Figure 7a gives the high-coercivity peak a near-ellipsoidal shape.

The high-field peak is curved in the FORC diagram and broadens vertically at high fields: such offset peaks have been described as "kidney" or "banana" shaped and have been previously reported in FORC diagrams of hematite [e.g., *Muxworthy et al.*, 2005; *Carvallo et al.*, 2006], monoclinic pyrrhotite [e.g., *Weaver et al.*, 2002], greigite [e.g., *Roberts et al.*, 2006], and magnetite when cooled through the Verwey transition in weak fields [*Smirnov*, 2007]. *Roberts et al.* [2010] observe that in all instances the magnetization is strongly controlled by magnetocrystalline anisotropy, but the mechanism to produce this signal has not been clearly articulated. Comparing the log-log remanence map and the linear FORC diagrams, we observe that the curvature and spreading of this feature are less pronounced in the log-log plot and the peak has a nearly ellipsoidal shape, which is elongated parallel to the diagonal. While the sampling of the remanence map is coarse, if this feature is truly regular on a log-log scale, it would indicate that both the offset and coercivity of this peak are a linear function of the applied field (see Figure 8c for another example).

The remanence maps of samples containing hematite lamellae in ilmenite (alone or in combination with hematite-hosted ilmenite) reveal that such ilmenite-hosted hematite have a characteristic signature. Sample 004–3 (Figure 8a) is an ilmenite ore containing titanohematite lamellae that commonly range down to the nanoscale [*McEnroe et al.*, 2002]. Volumetrically minor first-generation titanohematite lamellae (≤ 3 μm) contain minor ilmenite lamellae; however, later and much smaller generations rarely contain ilmenite. As in OSW1–2, there is an elongated peak offset below the diagonal, which is centered near 80 mT and is relatively weak. The stronger signal is along the diagonal, which accounts for all signal above ≈ 200 mT and extends well over 300 mT. Within the resolution of the measurement, there is no spread off the diagonal, which according to Preisach theory indicates that these particles are nonbiased uniaxial recorders.

Sample AL7B, a more iron-rich hemo-ilmenite ore comprising titanohematite-hosted ilmenite lamellae in addition to ilmenite-hosted titanohematite, also shows this discrete signal along the diagonal (Figure 8b). The coercivity of the sample is yet higher, with effectively no IRM acquired at fields less than 100 mT, the 90th percentile around 650 mT and measurable signal over 1 T. The offset peak below the diagonal is elongated, but nonellipsoidal, and clearly distinct from that along the diagonal. The strongest peaks in the offset
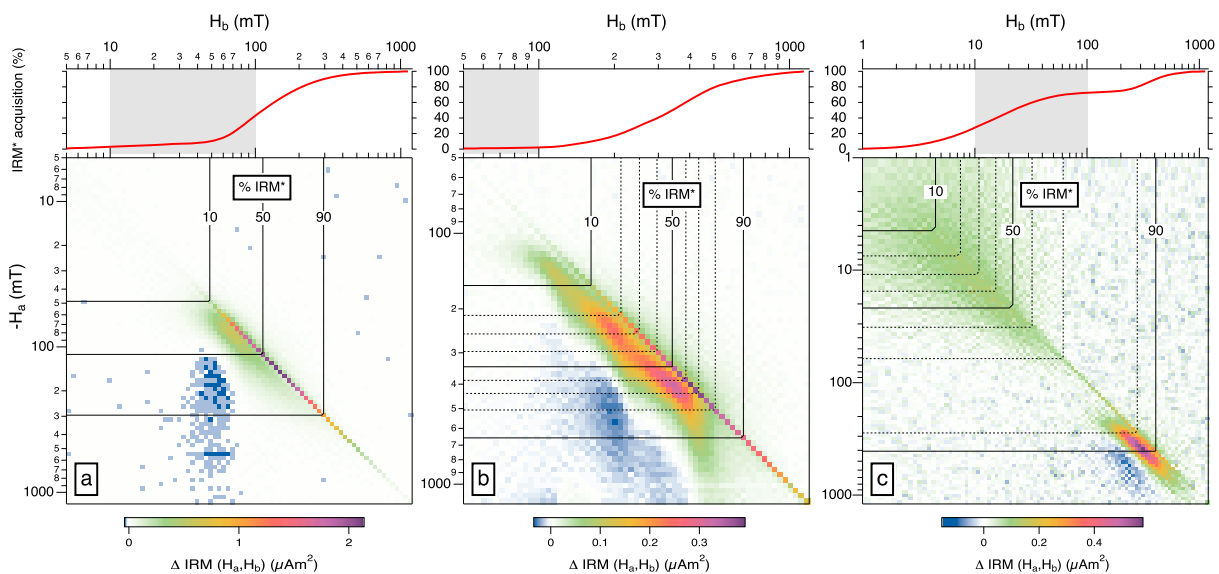
Figure 8. (a) Sample 004-3, a hemo-ilmenite ore with hematite lamellae ranging from the microscale to nanoscale, is dominated by signal along the diagonal, indicating nonbiased magnetic carriers. The offset peak associated with the presence of hematite is weak and centered around 80 mT. (b) AL7b from Allard Lake. Hemo-ilmenite showing two magnetic phases, both with extremely high coercivities (>100 mT). The diagonal distribution has a peak around 400 mT and extends at least to the maximum field in the instrumental setup (1.2 T). The off-diagonal distribution appears as two overlapping offset peaks with modal values around 200 and 400 mT. (c) Sample S11-8 from Sweden contains magnetite, and titanohematite and ilmenite, both with nanoscale exsolution. The distribution has three distinct phases. The soft phase has a lower cutoff of its coercivity near 2 mT, extends up to about 80 mT, and contains more than 50% of the total IRM. The two hard phases resemble those of AL7b, although their coercivities are some 10% lower.

signal qualitatively appear as at least two partially overlapping distributions, with maximum values at ≈200 and 400 mT. The multiple coercivity distributions in this characteristic Ti-hematite signal (likely modified by the lamellar magnetism created by the ilmenite precipitates within it) may result either from the crystallographic control of exsolution lamellae orientations within their millimeter-scale host, or intrinsic differences in magnetic response, potentially due to different generations of exsolution and their influence on the interface magnetism. Despite the multipeak morphology, the offset distribution remains broadly parallel to the diagonal in log-log space.

The remanence map shown in Figure 8c is that of S11–8, which with titanohematite-hosted ilmenite, ilmenite-hosted titanohematite, and coexisting magnetite, contains the most complex mineralogy of these samples. Each phase can be identified on the remanence map. Up to 70% of the IRM is held by the magnetite phase, which has a coercivity ranging from ≈2 to 80 mT and is spread off the diagonal with a negative bias; qualitatively, this distribution resembles the pure magnetite carriers examined in Figure 6. The signal along the diagonal, similar to that shown in Figures 8a and 8b is visible from 50 to at least 400 mT, where it overlaps the offset peak below the diagonal. In this sample, the offset peak is ellipsoidal and parallel to the diagonal, and is accompanied by a weak elongated negative trough. This phase accounts for over 20% of the IRM and has a coercivity distribution from 200 to 1000 mT.

Summing the magnetization of low-coercivity magnetite, diagonal, and offset hematite peak regions of the remanence map according to equation (5) of these multiphase samples allows the contribution of remanence distributions adjacent to each other on the Preisach map to be separated, shown in Table 1. These calculations agree well with microscopy observations of the microstructure: 004–3 contains the hematite in ilmenite exsolution and has a stronger relative contribution of the hematite signal along the diagonal compared to AL7b and S11–8. Bulk susceptibility of S11–8 is 0.065 (SI), as compared to 0.01 for OSW1–2, which is reflected in the former's stronger magnetite signal. Also of note is the negative trough associated with the offset hematite peak: the total negative signal of this feature is consistently around 8% of the total IRM. The source of this trough cannot be directly explained by the SD mechanism outlined in *Newell* [2005], but it also might be related to a systematic slope difference across the switching fields of the average hysterons. In this case it would be a characteristic response of hematite to the mean internal field, because it is proportional to the total magnetization of the sample but independent of the strength of the hematite signal.
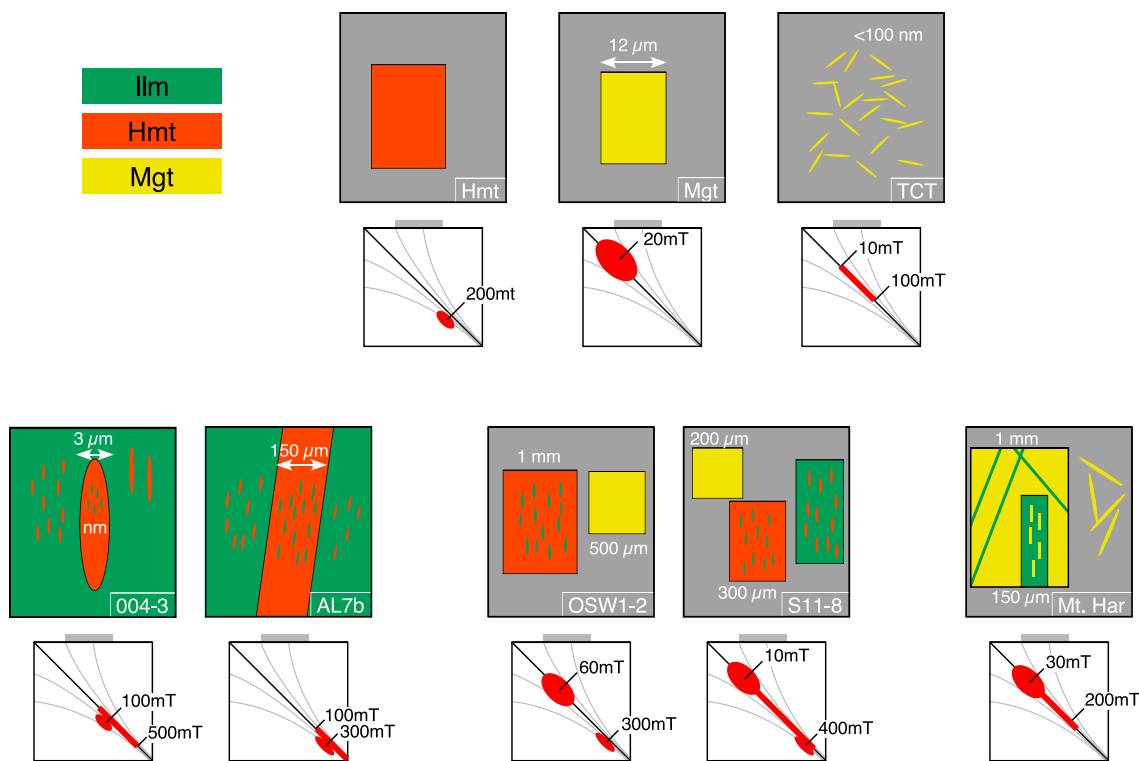
Figure 9. Schematic of the signatures of the different observed mineralogies upon the Preisach map. (top) Bulk hematite (coercivity estimated from *Muxworthy et al.* [2005]), synthetic PSD–MD Magnetite (Wright, 12 μm), SP–SD magnetite (Tiva Canyon Tuff). (bottom) Natural mixtures and microstructures as observed in the samples from Figures 5–8.

6. Discussion

6.1. Microstructure and Remanent Preisach Maps

Based on measurements of a suite of samples containing both varying oxide phases and varying microstructures, we find that some features on the remanence map serve as magnetic "fingerprints" for the domain state and mineralogy of the sample. Figure 9 presents schematically the results for the samples in this work, with characteristic signals and values on the remanence map highlighted. We observe that MD magnetite has a broad slightly asymmetric coercivity distribution within the interval $1\,\text{mT} \leq H_{cr} \leq 100\,\text{mT}$. Noninteracting SD magnetite has a sharp distribution along the diagonal with coercivities generally up to 100 mT and potentially a small component at higher fields. SD hematite — particularly that exsolved from ilmenite — has a distribution along the diagonal with coercivities exceeding 300 mT and may extend to 1 T or more. Bulk hematite in all but the most constrained SD size range has a characteristic subdiagonal distribution, which on a log-log scale is roughly ellipsoidal. Many of these observations agree with similar features known from classical Preisach or FORC diagrams but are more clearly resolved and distinguished due to the improved mapping. In the following sections some of these features are studied in more detail.

6.2. Coercivity Limits for SD Magnetite

There are limitations to the intrinsic coercivity distribution of a realistic natural ensemble of magnetite SD particles. The lower end originates from the rapid change of thermal stability near the SP-SD transition, where thermal activation overcomes the internal energy barrier due to shape-, magnetocrystalline-, or stress-induced anisotropy. Near the SP-SD transition the energy barrier is approximately $E_B = \max(0, KV - \log(t/\tau_0)\,k_B T)$, where K is the total anisotropy constant, V is particle volume, T is temperature, and k_B the Boltzmann constant, and the ratio t/τ_0 represents measurement timescale in relation to atomic relaxation time (typical laboratory $\log(t/\tau_0) = 23$; for geological timescale this value increases to over 40 [*Dunlop and Özdemir*, 1997]). For magnetite with a saturation magnetization of $M_s = 480\,\text{kA/m}$ this E_B is overcome by a field energy $E = M_s B_c V$. By setting $E = E_B$ one obtains

$$B_c = \max\left(0, \frac{K}{M_s} - 23\,\frac{k_B T}{M_s V}\right). \tag{6}$$
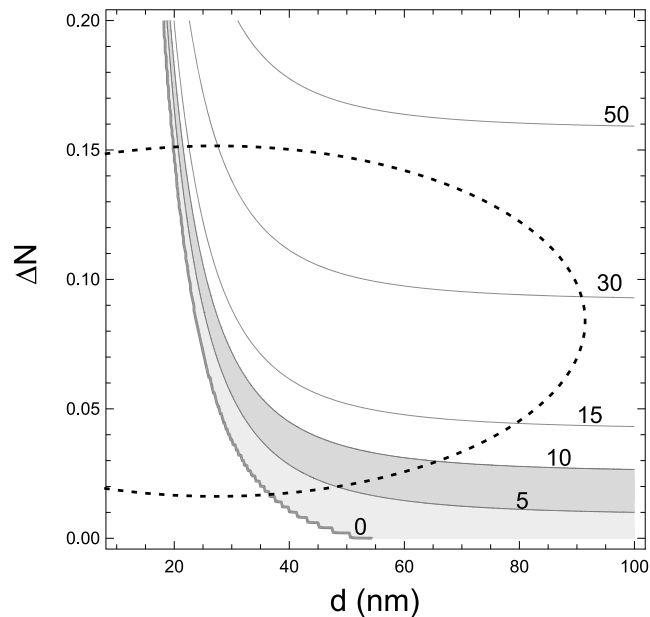
Figure 10. Theoretical contours for equal coercivity H_c as a function of grain diameter d and shape asymmetry in terms of the difference of demagnetizing factor ΔN in single-domain magnetite particles. The numbers at the contours are H_c in mT. Only for near-equidimensional particles with $\Delta N < 0.04$ a significant grain size fraction could have coercivities between 0 and 10 mT. Even in a narrow grain size distribution with realistic shape asymmetries (dashed line), only a small fraction of the observed coercivities will lie below 10 mT.

For a sufficiently wide volume distribution only a negligible fraction of particles have a volume for which

$$0 < 23 \frac{k_B T}{M_s V} < \frac{K^{\min}}{M_s}.$$

In this case the limiting lower coercivity $B_c^{\min}$ on the stable side of the SP-SD transition is about

$$B_c^{\min} \approx \frac{K^{\min}}{M_s}.$$

For magnetite particles

$$K = \frac{|K_1|}{12} + \frac{|K_1|}{4} \sin 2\phi + \frac{1}{2} \Delta N \mu_0 M_s^2,$$

where $K_1 \approx -1.34 \cdot 10^4$ J/m³ is the cubic anisotropy constant at room temperature and ϕ is the angle of the field within the (100) plane with $\phi = 0$ along [110] [*Butler and Banerjee*, 1975]. Coercivities of natural grain size distributions can be estimated by using (6) to create a diagram like Figure 10, which confirms that only for tiny elongations of $\Delta N < 0.04$ one may obtain a significant fraction of coercivity below 10 mT. Already small average elongations of $\Delta N > 0.04$ are sufficient to almost completely suppress the fraction with $B_c < 10$ mT, in very good agreement with observations of the Tiva Canyon tuff sample (Figure 5a). Note that increased anisotropy, for example, through internal stress fields, only increases this lower limit. Of course, magnetite can have much lower coercivities in the PSD-MD grain size region, and the upper end of the coercivity interval for pure SD magnetite is due to the onset of different magnetization reversal mechanisms and the breakdown of the SD state. In the same way a theoretical maximum limit of magnetite SD coercivity can be estimated for isotropic SD ensembles by setting the anisotropy K to the sum of magnetocrystalline and shape anisotropy ΔN and averaging over field directions ϕ which yields

$$K^{\max} = \frac{\pi + 6}{12\pi} |K_1| + \frac{1}{2} \Delta N \mu_0 M_s^2$$

for infinitely long needles $\Delta N = 1$ and if they lie in addition along a ⟨111⟩ direction this implies

$$B_c^{\max} = \frac{K^{\max}}{M_s} \approx 308 \text{ mT}.$$

For more realistic shapes with shape anisotropy $\Delta N \approx 1/3$ one obtains a reasonable upper limit of $B_c^{\text{max}*} \approx$ 100 mT. Also, the fact that nonhomogeneous reversal mechanisms in large SD grains create smaller coercivities suggests a lower estimate of $B_c^{\text{max}*}$. External influences, such as stress or exchange coupling to other magnetic phases, can add further terms to the anisotropy K, but the above simple estimates show that values of $B_c > 100$ mT in magnetite require very special circumstances. Therefore, the medium coercivity range of 10 mT – 100 mT coincides with the characteristic coercivities of common SD magnetite.

Several samples in this work exhibit signals from magnetite outside this SD coercivity range, which provides useful information for both fingerprinting remanence carriers and assessing the role of magnetite on magnetic recording on a geologic timescale in samples with complex mineralogies. The exceptionally high coercivity of the signal along the diagonal in the Mount Harcus samples (Figure 6), extending beyond the upper limit of even extremely elongated magnetite to nearly 400 mT, suggests that this signal is enhanced by factors relating to their host material, either stress generated at a coherent interface or exchange coupling with a magnetically ordered second phase.

By contrast, over 20% of the IRM of S11 – 8 (Figure 8c) has a coercivity less than 10 mT, suggesting that a significant proportion of the signal derives from non-SD behavior; microscopy of samples from this locality shows that the magnetite grains are single phase and hundreds of micrometer in diameter and therefore predicted to be MD. While over 50% of the IRM is held by the magnetite phase, the conclusion that the carrier is MD has implications which may vary depending if the analysis is to be used to inform a paleomagnetic or crustal anomaly study.

The limited coercivity range of magnetite is also helpful for differentiating signal along the diagonal that derives from magnetite from that associated with SD hematite. While there is some overlap in the coercivity distributions of the Mount Harcus samples (magnetite-bearing, Figure 6) and 004-3 (hematite, Figure 8a) significant signal along the diagonal in excess of $\approx$300 mT is a fingerprint of SD hematite, particularly that contained within an ilmenite host.

6.3. Origin of Asymmetric Distributions

Magnetostatic or exchange interaction, irreversible magnetization changes without magnetization jumps, and magnetocrystalline anisotropy are possible causes for asymmetric Preisach diagrams [e.g., *Girke*, 1960; *Pike et al.*, 2005; *Winklhofer and Zimanyi*, 2006]. For the Preisach hysteron interpretation to be strictly valid for an experimental Preisach diagram, the distribution must be symmetric about the diagonal, or "stable." With the exception of a few measurements (specifically, those presented in Figures 5a and 8a), such is not the case in the data sets in this work. This is primarily due to the asymmetry of the measurement protocol, as each IRM acquisition sequence applies a nonsaturating negative field following saturation in positive fields. This implies that the sample is always maximally magnetized in positive direction when measuring any rectangle in the Preisach map. This asymmetry could be taken into account by the adoption of a "moving model" that recalculates the Preisach distribution as a function of an effective field H_{eff} rather than the measured applied field H_{ext}, where

$$H_{\text{eff}} = H_{\text{ext}} + \gamma M, \tag{7}$$

where M is the current sample magnetization, and γ an experimentally derived interaction constant [*Della Torre*, 1965; *Hejda and Zelinka*, 1990; *Hejda et al.*, 1994]. The stability of an inferred Preisach distribution is likely to be improved by the moving model or by a symmetric measuring protocol (at the expense of greater measurement time), such as that proposed by *Carvallo et al.* [2005]. However, the qualitative presence of off-diagonal signals and the calculation of remanence percentiles are independent of the stability of the distribution.

In case of a positive interaction constant $\gamma > 0$ and positive M the effective field in (7) will be larger than H_{ext} such that upward switching will occur already at smaller H_{ext}, whereas downward switching in remanence carrying hysterons requires a more negative H_{ext}. In total, the hysteron moves to the left, or is negatively offset below the diagonal. However, because M saturates in a ferrimagnet, the ratio $\gamma M/H_{\text{ext}}$ approaches zero toward higher fields whereby the slope of a shifted diagonal distribution for $\gamma > 0$ is positive, as observed in the model of *Pike et al.* [1999, 2005]. Only for $\gamma < 0$ the slope of the corresponding upward shifted diagonal distribution is negative. The observed behavior of hematite therefore appears paradoxical because it shows at the same time a negative bias, indicating $\gamma > 0$, and a negative slope as known from $\gamma < 0$.
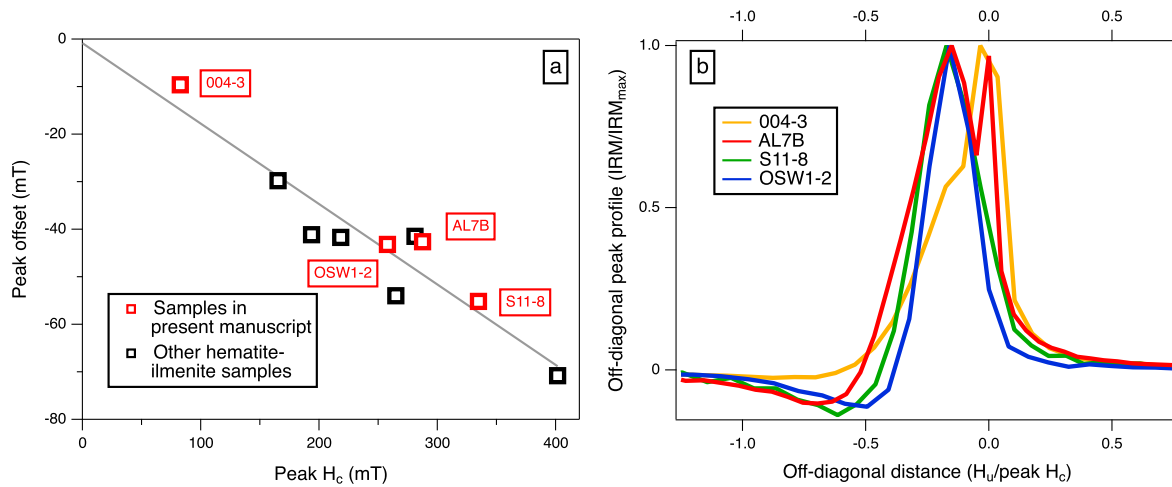
Figure 11. Off-diagonal peak position in hematite-bearing samples. (a) Peak offset versus peak coercivity indicates a linear relation $H_{off} \approx \beta H_c$ with $\beta = -0.17 \pm 0.02$. (b) Peak profiles perpendicular to main diagonal in relative units (H_u/peak H_c) have similar shapes. Samples 004–3 and AL7b also show the detached peak on the diagonal (0 in relative units), which is not present or too weak at this coercivity to resolve in other samples.

One possibility to accommodate these contradictory trends results from hematite's spontaneous and field-induced spin canting, both of which will react to any field source within the hematite host and create strongly interacting local magnetizations $M_{loc} = \chi^* H_{loc}$. If the local field H_{loc} is in turn created by hard magnetic moments (e.g., defect or imbalanced moments) which are proportional to the external field H_{ext}, a very strong intrinsic magnetostatic coupling between these moments gives rise to an effective field

$$H_{eff} = H_{ext} + \gamma M_{loc} = H_{ext} + \gamma \chi^* H_{loc} = (1 + \beta) H_{ext}, \qquad (8)$$

that is proportional to the external field and can act either as shielding ($\beta < 0$) or amplification ($\beta > 0$). The proportionality factor $(1 + \beta)$ depends on intrinsic properties, such as χ^*, and also on the distribution and size of the embedded hard moments. This type of interaction could explain the constant offset of the hematite distribution in the log-log Preisach map. From the offset one can derive an estimate of the interaction coefficient β, which for hematite hosts appears to yield a consistent $\beta \approx -0.17 \pm 0.02$ independent of the coercivity of the hematite phase (Figure 11a). This value appears to be a fingerprint of magnetic moments embedded in sufficiently large hematite hosts. Profiles through the center of the peak and perpendicular to the diagonal (i.e., H_u in rotated FORC space, presented in Figure 11b) show that the relative location of the peak remains constant, while their width and location of the negative trough associated with the hematite peak may vary.

As observed above, offset peaks in FORC diagrams have been reported in a variety of natural materials (pyrrhotite, greigite, and single-phase hematite) that have, in common, strong magnetocrystalline anisotropy that dominates switching behavior. *Harrison and Lascu* [2014] were also able to replicate an offset peak and associated negative trough, both with a negative slope, in simulations of SD particles with cubic anisotropy alone. In SD particles where magnetocrystalline anisotropy is dominant, multiple magnetization states are possible intermediate to plus or minus saturation, which if measured as a minor loop may have switching fields that are not equal and opposite [*Usov and Peschany*, 1997]. The asymmetry of such minor loops gives rise to FORC diagrams with offset features. The ilmenite-bearing hematite samples presented in this study are dominantly MD, in which case the strong magnetocrystalline into the basal plane, and the sixfold easy axes within it, could generate similar intermediate magnetic states by controlling the nucleation and denucleation of domains in proscribed crystallographic orientations. However, it is less clear how such a mechanism would lead to asymmetric minor loops when the switching mechanism is purely domain wall translation, which is also expected to be recorded in measurements of MD materials. The role of anisotropy in single-phase hematite and embedded moments in multiphase samples is the subject of ongoing research.

6.4. Hematite-Ilmenite Lamellae

Ilmenite lamellae in hematite hosts are prime examples of the interaction effect proposed above, as the ferrimagnetic interface of the phases serve as magnetic moments embedded in hematite. The case of hematite lamellae in ilmenite hosts is interesting because they display a completely different behavior.

The remanence-carrying hematite lamellae interact with the paramagnetic host only in that they are impacted by stress due to elastic and plastic deformations in response to the strain at the ilmenite-hematite interfaces [*Merrill*, 1968; *Shive and Butler*, 1969]. In case of nanoscale lamellae with strain-limited growth, the elastic contribution will probably be higher than in case of dominant plastic deformation in larger lamellae studied by *Shive and Butler* [1969]. To estimate an upper limit of coercivity of nanoscale lamellae, we assume that the hematite-ilmenite interface shares a common $\langle 001 \rangle$ plane that differs by about $\Delta\epsilon = 5\%$ in lattice dimensions along the c axis. Lamellar moments in hematite result from uncompensated spins at the lamellae interfaces. A rough order-of-magnitude approximation of the average magnetization is given by

$$\bar{M}_s = \frac{M_{sub}\, c\, A}{V},$$

where $M_{sub} \approx 920$ kA/m is the sublattice magnetization of hematite [*Morrish*, 1994, Table 4.2], $c \approx 1.4$ nm is the height of the unit cell, V the volume, and A the interface surface area of a lamella. The anisotropy energy is dominated by magnetoelastic (me) interaction, which can be crudely estimated by

$$K_{me} \approx \lambda\, \sigma_{strain},$$

where $\lambda \approx 10^{-5}$ is a magnetostriction estimate for hematite [*Morrish*, 1994, Table 7.1], and the purely elastic stress due to lattice strain is approximately

$$\sigma_{strain} \approx \Delta\epsilon\, c_{11},$$

where $c_{11} \approx 240$ GPa [*Morrish*, 1994, Table 7.1]. In case of disk-shaped cylindrical lamellae with radius r and height $h \ll r$, one has $A/V \approx 2/h$ which results in

$$B_c^{max} = \frac{K_{me}}{\bar{M}_s} \approx \frac{\lambda\, \Delta\epsilon\, c_{11}}{2\, M_{sub}}\, \frac{h}{c} \approx 70\,\text{mT}\, \frac{h}{c}.$$

For lamella thicknesses of about $h = 20$ nm as observed by *Kasama et al.* [2009] this leads to coercivities of up to 1 T. For thinner lamellae, or if a significant amount of plastic instead of elastic deformation occurs at the interfaces, the coercivity can be significantly smaller. For example, the much more sophisticated study by *Shive and Butler* [1969] focuses on stress fields of the periodic dislocation arrays induced by plastic deformation and obtain maximal coercivities of 140 mT. They also invoked strong domain wall pinning, which does not apply to SD states as highest coercivity carriers. Nanoscale lamellae that are far smaller than any proposed size for the SD-MD transition [*Özdemir and Dunlop*, 2014 and references therein] are therefore rather expected to show substantially higher coercivities.

The high coercivities related to the sharply defined diagonal distribution in the Preisach maps of Figure 8 suggest that a fraction of the remanence carriers in these samples are unusually stable single-domain particles. The previous calculation shows that ilmenite-hosted SD hematite lamellae, which are abundant in these samples, can explain these high coercivities. In addition, the occurrence of highly strained lamellae is supported by observations of large strain shadows surrounding the lamellae in TEM images of the samples in Figure 8 [*McEnroe et al.*, 2002, 2004b, 2007]. High coercivity due to excessive strain also implies a considerable lowering of the SP-SD threshold in ilmenite-hosted hematite lamellae such that most of the nanoscale lamellae can carry a stable remanence at room temperature.

7. Conclusions

The previous experimental and theoretical results lead to the following conclusions:

1. The adaptation of remanent Preisach diagrams to use logarithmic measurement and plotting improves the dynamic range of sensitivity over induced measurements to synchronously resolve high-coercivity remanence carriers with coexisting MD grains. The nonlinear field steps make the protocol time efficient and provide fine resolution of MD processes at weak applied fields, while the mapping of total magnetization rather than magnetization density removes the necessity of smoothing. The method is well-suited for samples that have large volumes of MD material, whose induced magnetization signal dominates in-field measurements and creates the risk of loss-of-significance errors when trying to resolve much weaker remanence carriers.

2. Characteristic features on the remanence maps can be attributed to oxide morphologies and microstructures or nanostructures. Noninteracting SD magnetite and hematite subject to high stress from elastic strain in an ilmenite matrix generate a signal solely along the diagonal. These two phases appear to be experimentally well distinguished by their coercivity ranges. MD magnetite can be identified by an extensive spread off the diagonal and its coercivity distribution reaching well below 5 mT.

3. Any MD hematite matrix creates a characteristic peak which is offset below the diagonal on the remanence map. When displayed on a log-log scale, this (previously reported) feature assumes a regular ellipsoidal shape with a constant offset that is found to be ≈17% of the applied field. This hematite signal is proposed to be a shielding effect related to embedded moments in the host, which may arise from secondary phases or hard defect moments of the material itself.

4. The log-log remanence maps resolve features that may be difficult or impossible to observe in FORC or IRM acquisition analysis. Due to improved sensitivity and avoidance of smoothing artifacts, weak remanence features can be identified more clearly in discrete regions of the remanence map.

The remanent Preisach method is a useful quantitative tool to study remanent magnetization processes in complex mixtures of magnetic minerals and a method to efficiently acquire and present high-resolution data unbiased by artificially large induced magnetizations. While the technique is IRM based, it will be of interest to methodologically link the observed patterns to corresponding features of NRM carriers. This will help to identify primary NRM carriers and provide reliable data for future theoretical studies to predict, interpret, and model details of the observed maps in terms of interacting magnetic minerals and their microstructures and nanostructures.

Appendix A: Rescaling Preisach Maps to Logarithmic Preisach Distributions

A main goal of the above outlined Preisach mapping approach is to directly present the data without introducing processing steps that could introduce unnecessary artificial features or detract from ease of comprehension. Ramon Egli convinced us that there are equally valid arguments for a more universal representation that enables quantitative analysis independent of details of the measurement protocol, including traditional Preisach distributions and FORC functions. As discussed in the main text, one directly obtains the Preisach distribution when dividing our equation (3) by $(H_i - H_{i-1}) \times (H_j - H_{j-1})$. In his insightful and helpful review, Dr. Egli pointed out that deviations from exact logarithmic sampling of the fields, pronounced at small field values due to the hyperbolic sine function used in measurement (2), can be very simply corrected for. His argument is based on the observation that our Preisach maps up to a constant factor essentially are finite difference approximations of the mixed derivatives of the logarithmically scaled magnetization function. From the magnetization function $M(H_a, H_b)$ the Preisach distribution is obtained as

$$p(H_a, H_b) = -\frac{1}{2} \frac{\partial^2}{\partial H_a \, \partial H_b} M(H_a, H_b).$$

The variables in our Preisach map ideally are the logarithms $L_{a,b} = \log H_{a,b}$, for which the logarithmically scaled magnetization function becomes $M_{\log}(L_a, L_b) = M(H_a, H_b)$, whereby the mixed second derivative is the logarithmic Preisach distribution

$$p_{\log}(L_a, L_b) = -\frac{1}{2} \frac{\partial^2}{\partial L_a \, \partial L_b} M_{\log}(L_a, L_b) = H_a H_b \, p(H_a, H_b).$$

Independent of the details of a sufficiently dense sampling scheme, the finite difference approximation to $p_{\log}(L_a, L_b)$ based on neighboring upper and lower values $\left(L_{a,b}^{+,-} = \log H_{a,b}^{+,-} \right)$ is

$$
\begin{aligned}
p_{\log}(L_a, L_b) &\approx \frac{1}{2} \frac{M_{\log}\left(L_a^+, L_b^+\right) + M_{\log}\left(L_a^-, L_b^-\right) - M_{\log}\left(L_a^+, L_b^-\right) - M_{\log}\left(L_a^-, L_b^+\right)}{\left(L_a^+ - L_a^-\right)\left(L_b^+ - L_b^-\right)} \\
&\approx \frac{\left(H_a^+ + H_a^-\right)\left(H_b^+ + H_b^-\right)}{\left(H_a^+ - H_a^-\right)\left(H_b^+ - H_b^-\right)} \frac{M\left(H_a^+, H_b^+\right) + M\left(H_a^-, H_b^-\right) - M\left(H_a^+, H_b^-\right) - M\left(H_a^-, H_b^+\right)}{8},
\end{aligned}
\tag{A1}
$$

which apart from the first factor and the scaling factor 8 corresponds to equation (3). It is therefore easy to rescale Preisach maps to logarithmic Preisach distributions which have a universal definition and we encourage doing so if detailed quantitative comparison of different samples is required. We were initially worried that

the denominator $(H_a^+ - H_a^-)(H_b^+ - H_b^-)$ would cause undesirable amplification of the Preisach distribution near the origin. However, such is not the case for our data sets and the qualitative relationships described in this work are unaffected. Like Preisach maps, the $p_{\log}(L_a, L_b)$ distribution intrinsically weighs remanences proportional to their coercivity which in our opinion is a good compromise to visualize NRM-related features of rocks. The full data sets for all samples are available from the corresponding author to enable curious researchers to compare the effects of different representations.

References

Austin, J., D. Hillan, P. W. Schmidt, and C. Foss (2014), Understanding magnetism in the Giles Complex, Musgrave Block, SA, *Preview*, *2014*(171), 41–44, doi:10.1071/PVv2014n171p41.

Balsley, J. R., and A. F. Buddington (1958), Iron-titanium oxide minerals, rocks, and aeromagnetic anomalies of the Adirondack area, New York, *Econ. Geol.*, *53*(7), 777–805, doi:10.2113/gsecongeo.53.7.777.

Bate, G. (1962), Statistical stability of the Preisach diagram for particles of γ-Fe$_2$O$_3$, *J. Appl. Phys.*, *33*(7), 2263–8, doi:10.1063/1.1728942.

Becker, R., and W. Döring (1939), Ferromagnetismus, doi:10.1007/978-3-642-47366-1.

Brok, E., M. Sales, K. Lefmann, L. T. Kuhn, W. F. Schmidt, B. Roessli, P. Robinson, S. A. McEnroe, and R. J. Harrison (2014), Experimental evidence for lamellar magnetism in hemo-ilmenite by polarized neutron scattering, *Phys. Rev. B*, *89*(5), 054430, doi:10.1103/PhysRevB.89.054430.

Brown, L. L., and S. A. McEnroe (2012), Paleomagnetism and magnetic mineralogy of Grenville metamorphic and igneous rocks, Adirondack Highlands, USA, *Precambrian Res.*, *212–213*, 57–74, doi:10.1016/j.precamres.2012.04.012.

Butler, R. F., and S. K. Banerjee (1975), Theoretical single-domain grain size range in magnetite and titanomagnetite, *J. Geophys. Res.*, *80*, 4049–4058.

Carvallo, C., D. J. Dunlop, and Ö. Özdemir (2005), Experimental comparison of FORC and remanent Preisach diagrams, *Geophys. J. Int.*, *162*(3), 747–754, doi:10.1111/j.1365-246X.2005.02688.x.

Carvallo, C., A. R. Muxworthy, and D. J. Dunlop (2006), First-order reversal curve (FORC) diagrams of magnetic mixtures: Micromagnetic models and measurements, *Phys. Earth Planet. Inter.*, *154*(3–4), 308–322, doi:10.1016/j.pepi.2005.06.017.

Daniel, E. D., and I. Levine (1960), Experimental and theoretical investigation of the magnetic properties of iron oxide recording tape, *J. Acoust. Soc. Am.*, *32*(1), 1–15, doi:10.1121/1.1907872.

Day, R., M. D. Fuller, and V. A. Schmidt (1977), Hysteresis properties of titanomagnetites—Grain-size and compositional dependence, *Phys. Earth Planet. Inter.*, *13*(4), 260–267, doi:10.1016/0031-9201(77)90108-X.

Della Torre, E. (1965), Measurements of interaction in an assembly of γ-iron oxide particles, *J. Appl. Phys.*, *36*(2), 518–522, doi:10.1063/1.1714022.

Della Torre, E. (1966), Effect on interaction on the magnetization of single-domain particles, *IEEE Trans. Audio Electroacoust.*, *14*, 86–93.

Dunlop, D. J. (2002), Theory and application of the Day plot (M$_{rs}$/M$_s$ versus H$_{cr}$/H$_c$) 1. Theoretical curves and tests using titanomagnetite data, *J. Geophys. Res.*, *107*(B3), 2056, doi:10.1029/2001JB000486.

Dunlop, D. J., and Ö. Özdemir (1997), *Rock Magnetism: Fundamentals and Frontiers*, Cambridge Univ. Press, Cambridge, U. K.

Dunlop, D. J., and G. F. West (1969), An experimental evaluation of single domain theories, *Rev. Geophys.*, *7*(4), 709–757.

Dunlop, D. J., M. F. Westcott-Lewis, and M. E. Bailey (1990), Preisach diagrams and anhysteresis: Do they measure interactions?, *Phys. Earth Planet. Inter.*, *65*, 62–77.

Dyar, M. D., S. A. McEnroe, E. Murad, L. L. Brown, and H. Schiellerup (2004), The relationship between exsolution and magnetic properties in hemo-ilmenite: Insights from Mossbauer spectroscopy with implications for planetary magnetic anomalies, *Geophys. Res. Lett.*, *31*(4), L04608, doi:10.1029/2003GL019076.

Egli, R. (2003), Analysis of the field dependence of remanent magnetization curves, *J. Geophys. Res.*, *108*, B22081, doi:10.1029/2002JB002023.

Egli, R. (2013), VARIFORC: An optimized protocol for calculating non-regular first-order reversal curve (FORC) diagrams, *Global Planet. Change*, *110*, 302–320, doi:10.1016/j.gloplacha.2013.08.003.

Egli, R., A. P. Chen, M. Winklhofer, K. P. Kodama, and C.-S. Horng (2010), Detection of noninteracting single domain particles using first-order reversal curve diagrams, *Geochem. Geophys. Geosyst.*, *11*(1), Q01Z11, doi:10.1029/2009GC002916.

Fabian, K., and T. von Dobeneck (1997), Isothermal magnetization of samples with stable Preisach function: A survey of hysteresis, remanence, and rock magnetic parameters, *J. Geophys. Res.*, *102*(B8), 17,659–17,677, doi:10.1029/97JB01051.

Frandsen, C., S. Mørup, and S. A. McEnroe (2007), Magnetic phases in hemo-ilmenite: Insight from low-velocity and high-field Mössbauer spectroscopy, *Geophys. Res. Lett.*, *34*, 1–5, doi:10.1029/2006GL029063.

Girke, H. (1960), Der Einfluß innerer magnetischer Kopplungen auf die gestalt der Preisach-Funktionen hochpermeabler Materialien, *Z. Angew. Phys.*, *11*, 502–508.

Harrison, R. J. (2006), Microstructure and magnetism in the ilmenite-hematite solid solution: A Monte Carlo simulation study, *Am. Mineral.*, *91*(7), 1006–1023, doi:10.2138/am.2006.2008.

Harrison, R. J., and J. M. Feinberg (2008), FORCinel: An improved algorithm for calculating first-order reversal curve distributions using locally weighted regression smoothing, *Geochem. Geophys. Geosyst.*, *9*(5), Q05016, doi:10.1029/2008GC001987.

Harrison, R. J., and I. Lascu (2014), FORCulator: A micromagnetic tool for simulating first-order reversal curve diagrams, *Geochem. Geophys. Geosyst.*, *15*, 4671–4691, doi:10.1002/2014GC005582.

Hejda, P., and T. Zelinka (1990), Modelling of hysteresis processes in magnetic rock samples using the preisach diagram, *Phys. Earth Planet. Inter.*, *63*, 32–40.

Hejda, P., E. Petrovsky, and T. Zelinka (1994), The Preisach diagram, Wohlfarth's remanence formula and magnetic interactions, *IEEE Trans. Magn.*, *30*(2), 896–898, doi:10.1109/20.312439.

Heslop, D., and A. R. Muxworthy (2005), Aspects of calculating first-order reversal curve distributions, *J. Magn. Magn. Mater.*, *288*, 155–167, doi:10.1016/j.jmmm.2004.09.002.

Heslop, D., G. McIntosh, and M. J. Dekkers (2004), Using time- and temperature-dependent Preisach models to investigate the limitations of modelling isothermal remanent magnetization acquisition curves with cumulative log Gaussian functions, *Geophys. J. Int.*, *157*(1), 55–63, doi:10.1111/j.1365-246X.2004.02155.x.

Heslop, D., A. P. Roberts, and L. Chang (2014), Characterizing magnetofossils from first-order reversal curve central ridge signatures, *Geochem. Geophys. Geosyst.*, *15*, 2170–2179, doi:10.1002/2014GC005291.

Ivanov, V. A., I. A. Khaburzaniya, and L. Y. Sholpo (1981), Use of Preisach diagram for diagnosis of single- and multi-domain grains in rock samples, *Izv. Earth Phys.*, *17*, 36–43.

Kasama, T., S. A. McEnroe, N. Ozaki, T. Kogure, and A. Putnis (2004), Effects of nanoscale exsolution in hematite-ilmenite on the acquisition of stable natural remanent magnetization, *Earth Planet. Sci. Lett.*, *224*(3–4), 461–475, doi:10.1016/j.epsl.2004.05.027.

Kasama, T., R. E. Dunin-Borkowski, T. Asaka, R. J. Harrison, R. K. K. Chong, S. A. McEnroe, E. T. Simpson, Y. Matsui, and A. Putnis (2009), The application of Lorentz transmission electron microscopy to the study of lamellar magnetism in hematite-ilmenite, *Am. Mineral.*, *94*(2–3), 262–269, doi:10.2138/am.2009.2989.

Krasa, D., C. Heunemann, R. Leonhardt, and N. Petersen (2003), Experimental procedure to detect multidomain remanence during Thellier-Thellier experiments, *Phys. Chem. Earth*, *28*(16–19), 681–687, doi:10.1016/S1474-7065(03)00122-0.

Kumari, M., A. M. Hirt, R. Uebe, D. Schüler, É. Tompa, M. Posfai, W. Lorenz, C. Ahrentorp, C. Jonasson, and C. Johansson (2015), Experimental mixtures of superparamagnetic and single domain magnetite with respect to Day-Dunlop plots, *Geochem. Geophys. Geosyst.*, *16*, 1739–1752, doi:10.1002/2015GC005744.

Lascu, I., R. J. Harrison, Y. Li, J. R. Muraszko, J. E. T. Channell, A. M. Piotrowski, and D. A. Hodell (2015), Magnetic unmixing of first-order reversal curve diagrams using principal component analysis, *Geochem. Geophys. Geosyst.*, *16*, doi:10.1002/2015gc005909.

Mayergoyz, I. (1988), Vector Preisach hysteresis models, *J. Appl. Phys.*, *63*, 2995–3000.

McCammon, C. A., S. A. McEnroe, P. Robinson, K. Fabian, and B. P. Burton (2009), High efficiency of natural lamellar remanent magnetisation in single grains of ilmeno-hematite calculated using Mossbauer spectroscopy, *Earth Planet. Sci. Lett.*, *288*(1–2), 268–278, doi:10.1016/j.epsl.2009.09.030.

McEnroe, S. A., and L. L. Brown (2000), A closer look at remanence-dominated aeromagnetic anomalies: Rock magnetic properties and magnetic mineralogy of the Russell Belt microcline-sillimanite gneiss, northwest Adirondack Mountains, New York, *J. Geophys. Res.*, *105*(B7), 16,437–16,456, doi:10.1029/2000JB900051.

McEnroe, S. A., R. J. Harrison, P. Robinson, U. Golla-Schindler, and M. J. Jercinovic (2001a), Effect of fine-scale microstructures in titanohematite on the acquisition and stability of natural remanent magnetization in granulite facies metamorphic rocks, southwest Sweden: Implications for crustal magnetism, *J. Geophys. Res.*, *106*(B12), 30,523–30,546, doi:10.1029/2001JB000180.

McEnroe, S. A., P. Robinson, and P. T. Panish (2001b), Aeromagnetic anomalies, magnetic petrology, and rock magnetism of hemo-ilmenite-and magnetite-rich cumulate rocks from the Sokndal Region, South Rogaland, Norway, *Am. Mineral.*, *86*(11–12), 1447–1468, doi:10.2138/am-2001-11-1213.

McEnroe, S. A., R. J. Harrison, P. Robinson, and F. Langenhorst (2002), Nanoscale haematite-ilmenite lamellae in massive ilmenite rock: An example of 'lamellar magnetism' with implications for planetary magnetic anomalies, *Geophys. J. Int.*, *151*(3), 890–912, doi:10.1046/j.1365-246X.2002.01813.x.

McEnroe, S. A., J. R. Skilbrei, P. Robinson, F. Heidelbach, F. Langenhorst, and L. L. Brown (2004a), Magnetic anomalies, layered intrusions and Mars, *Geophysical Research Letters*, *31*(19), L19601, doi:10.1029/2004GL020640.

McEnroe, S. A., F. Langenhorst, P. Robinson, G. D. Bromiley, and C. Shaw (2004b), What is magnetic in the lower crust?, *Earth Planet. Sci. Lett.*, *226*(1–2), 175–192, doi:10.1016/j.epsl.2004.07.020.

McEnroe, S. A., P. Robinson, F. Langenhorst, C. Frandsen, M. P. Terry, and T. Boffa Ballaran (2007), Magnetization of exsolution intergrowths of hematite and ilmenite: Mineral chemistry, phase relations, and magnetic properties of hemo-ilmenite ores with micron- to nanometer-scale lamellae from Allard Lake, Quebec, *J. Geophys. Res.*, *112*(B10), B10103, doi:10.1029/2007JB004973.

McEnroe, S. A., K. Fabian, P. Robinson, C. Gaina, and L. L. Brown (2009a), Crustal magnetism, lamellar magnetism and rocks that remember, *Elements*, *5*(4), 241–246, doi:10.2113/gselements.5.4.241.

McEnroe, S. A., L. L. Brown, and P. Robinson (2009b), Remanent and induced magnetic anomalies over a layered intrusion: Effects from crystal fractionation and magma recharge, *Tectonophysics*, *478*(1–2), 119–134, doi:10.1016/j.tecto.2008.11.021.

Merrill, R. (1968), A possible source for coercivity of ilmenite-hematite minerals, *J. Geomagn. Geoelec.*, *20*(3), 181–185, doi:10.5636/jgg.20.181.

Morrish, A. H. (1994), *Canted Antiferromagnetism: Hematite*, World Sci., Singapore.

Muxworthy, A. R., and D. Heslop (2011), A Preisach method for estimating absolute paleofield intensity under the constraint of using only isothermal measurements: 1. Theoretical framework, *J. Geophys. Res.*, *116*, B04102, doi:10.1029/2010JB007843.

Muxworthy, A. R., J. G. King, and D. Heslop (2005), Assessing the ability of first-order reversal curve (FORC) diagrams to unravel complex magnetic signals, *J. Geophys. Res.*, *110*, B01105, doi:10.1029/2004JB003195.

Néel, L. (1944), Effet des cavités et des inclusions sur le champ coercitif, *Cah. Phys.*, *25*, 21–44.

Newell, A. J. (2005), A high-precision model of first-order reversal curve (FORC) functions for single-domain ferromagnets with uniaxial anisotropy, *Geochem. Geophys. Geosyst.*, *6*(5), Q05010, doi:10.1029/2004GC000877.

Özdemir, Ö., and D. J. Dunlop (2014), Hysteresis and coercivity of hematite, *J. Geophys. Res. Solid Earth*, *119*(4), 2582–2594, doi:10.1002/2013JB010739.

Pentcheva, R., and H. S. Nabi (2008), Interface magnetism in Fe2O3/FeTiO3 heterostructures, *Phys. Rev. B.*, *77*(17), 172405, doi:10.1103/PhysRevB.77.172405.

Pike, C. R., A. P. Roberts, and K. L. Verosub (1999), Characterizing interactions in fine magnetic particle systems using first order reversal curves, *J. Appl Phys.*, *85*(9), 6660–6667, doi:10.1063/1.370176.

Pike, C. R., A. P. Roberts, M. J. Dekkers, and K. L. Verosub (2001), An investigation of multi-domain hysteresis mechanisms using forc diagrams, *Phys.Earth Planet. Inter.*, *126*(1–2), 11–25.

Pike, C. R., C. A. Ross, R. T. Scalettar, and G. T. Zimanyi (2005), First-order reversal curve diagram analysis of a perpendicular nickel nanopillar array, *Phys. Rev. B*, *71*(13), 134407, doi:10.1103/PhysRevB.71.134407.

Preisach, F. (1935), Über die magnetische Nachwirkung, *Z. Phys. A: Hadrons Nucl.*, *94*(5), 277–302.

Roberts, A. P., C. R. Pike, and K. L. Verosub (2000), First-order reversal curve diagrams: A new tool for characterizing the magnetic properties of natural samples, *J. Geophys. Res.*, *105*(B12), 28,461–28,475, doi:10.1029/2000JB900326.

Roberts, A. P., Q. Liu, C. J. Rowan, L. Chang, C. Carvallo, J. Torrent, and C.-S. H. horng (2006), Characterization of hematite (alpha-Fe2O3), goethite (alpha-FeOOH), greigite (Fe3S4), and pyrrhotite (Fe7S8) using first-order reversal curve diagrams, *J. Geophys. Res.*, *111*, B12S35, doi:10.1029/2006JB004715.

Roberts, A. P., F. Florindo, J. C. Larrasoaña, A. R. Muxworthy, and X. Zhao (2010), Complex polarity pattern at the former Plio-Pleistocene global stratotype section at Vrica (Italy): Remagnetization by magnetic iron sulphides, *Earth Planet. Sci. Lett.*, *292*(1–2), 98–111, doi:10.1016/j.epsl.2010.01.025.

Roberts, A. P., D. Heslop, and X. Zhao (2014), Understanding fine magnetic particle systems through use of first-order reversal curve diagrams, *Rev. Geophys.*, *52*, 557–602, doi:10.1002/2014RG000462.

Robertson, D. J., and D. E. France (1994), Discrimination of remanence-carrying minerals in mixtures, using isothermal remanent magnetization acquisition curves, *Phys. Earth Planet. Inter.*, *82*(3–4), 223–234, doi:10.1016/0031-9201(94)90074-4.

Robinson, P. (2006), Fe^{2+}/Fe^{3+} charge ordering in contact layers of lamellar magnetism: Bond valence arguments, *Am. Mineral.*, *91*(1), 67–72, doi:10.2138/am.2006.2012.

Robinson, P., R. J. Harrison, S. A. McEnroe, and R. B. Hargraves (2002), Lamellar magnetism in the haematite-ilmenite series as an explanation for strong remanent magnetization, *Nature*, *418*(6897), 517–520, doi:10.1038/nature00942.

Robinson, P., R. J. Harrison, S. A. McEnroe, and R. B. Hargraves (2004), Nature and origin of lamellar magnetism in the hematite-ilmenite series, *Am. Mineral.*, *89*(5–6), 725–747, doi:10.2138/am-2004-5-607.

Robinson, P., K. Fabian, S. A. McEnroe, and F. Heidelbach (2013), Influence of lattice-preferred orientation with respect to magnetizing field on intensity of remanent magnetization in polycrystalline hemo-ilmenite, *Geophys. J. Int.*, *192*(2), 514–536, doi:10.1093/gji/ggs046.

Robinson, P., S. A. McEnroe, N. Miyajima, K. Fabian, and N. S. Church (2016), Remanent magnetization, magnetic coupling, and interface ionic configurations of intergrown rhombohedral and cubic Fe-Ti oxides: A short survey, *Am. Mineral.*, *101*(3), 518–530, doi:10.2138/am-2016-5519.

Schlinger, C. M., D. R. Veblen, and J. G. Rosenbaum (1991), Magnetism and magnetic mineralogy of ash flow tuffs from Yucca Mountain, Nevada, *J. Geophys. Res.*, *96*(B4), 6035–6052, doi:10.1029/90JB02653.

Shive, P. N., and R. Butler (1969), Stresses and magnetostrictive effects of lamellae in the titanomagnetite and ilmenohematite series, *J. Geomagn. Geoelec.*, *21*(4), 781–796.

Smirnov, A. V. (2007), Effect of the magnetic field applied during cooling on magnetic hysteresis in the low-temperature phase of magnetite: First-order reversal curve (FORC) analysis, *Geochem. Geophys. Geosyst.*, *8*, Q08005, doi:10.1029/2007GC001650.

Stacey, F. D., and S. K. Banerjee (1974), *The Physical Principles of Rock Magnetism*, Elsevier Scientific Publ. Company, Amsterdam.

Stancu, A., P. Andrei, and L. Stoleriu (2006), Magnetic characterization of samples using first- and second-order reversal curve diagrams, *J. Appl. Phys.*, *99*(8), 08D702, doi:10.1063/1.2172539.

Stockhausen, H. (1998), Some new aspects for the modelling of isothermal remanent magnetization acquisition curves by cumulative log Gaussian functions, *Geophys. Res. Lett.*, *25*(12), 2217–2220, doi:10.1029/98GL01580.

Stoner, E., and E. P. Wohlfarth (1948), A mechanism of magnetic hysteresis in heterogeneous alloys, *Philos. Trans. R. Soc. London, Ser. A*, *240*(826), 599–642, doi:10.1098/rsta.1948.0007.

Usov, N. A., and S. E. Peschany (1997), Theoretical hysteresis loops for single-domain particles with cubic anisotropy, *J. Magn. Magn. Mater.*, *174*(3), 247–260, doi:10.1016/S0304-8853(97)00180-7.

Usui, Y., T. Shibuya, Y. Sawaki, and T. Komiya (2015), Rock magnetism of tiny exsolved magnetite in plagioclase from a Paleoarchean granitoid in the Pilbara Craton, *Geochem. Geophys. Geosyst.*, *16*(1), 112–125, doi:10.1002/2014GC005508.

Weaver, R., A. P. Roberts, and A. J. Barker (2002), A late diagenetic (syn-folding) magnetization carried by pyrrhotite: implications for paleomagnetic studies from magnetic iron sulphide-bearing sediments, *Earth Planet. Sci. Lett.*, *200*(3–4), 371–386, doi:10.1016/S0012-821X(02)00652-0.

Winklhofer, M., and G. T. Zimanyi (2006), Extracting the intrinsic switching field distribution in perpendicular media: A comparative analysis, *J. Appl. Phys.*, *99*(8), 08E710, doi:10.1063/1.2176598.

Winklhofer, M., R. K. Dumas, and K. Liu (2008), Identifying reversible and irreversible magnetization changes in prototype patterned media using first- and second-order reversal curves, *J. Appl. Phys.*, *103*(7), 07C518, doi:10.1063/1.2837888.

Worm, H.-U., and M. J. Jackson (1999), The superparamagnetism of Yucca Mountain Tuff, *J. Geophys. Res.*, *104*(B11), 25,415–25,425, doi:10.1029/1999JB900285.

Zelinka, T., P. Hejda, and V. Kropacek (1987), The vibrating-sample magnetometer and Preisach diagram, *Phys. Earth Planet. Inter.*, *46*(1–3), 241–246, doi:10.1016/0031-9201(87)90186-5.

Zhao, X., D. Heslop, and A. P. Roberts (2015), A protocol for variable-resolution first-order reversal curve measurements, *Geochem. Geophys. Geosyst.*, *16*(5), 1364–1377, doi:10.1002/2014GC005680.